UNIVERSITY OF CALIFORNIA,
IRVINE

Higher-Order Accurate Diffuse-Domain Methods for Partial Differential Equations with Dirichlet Boundary Conditions in Complex, Envolving Geometries

DISSERTATION

submitted in partial satisfaction of the requirements
for the degree of

DOCTOR OF PHILOSOPHY

in Mathematics

by

Fei Yu

Dissertation Committee:
Professor John Lowengrub, Chair
Professor Long Chen
Professor Hongkai Zhao

2018

DEDICATION

To my beloved parents and wife for their love, endless support and encouragement.

TABLE OF CONTENTS

LIST OF FIGURES

LIST OF TABLES

ACKNOWLEDGMENTS

I am very grateful for my advisor, Professor John Lowengrub, for his assistance, guidance and encouragement through my PhD journey. I would also like to thank my committee members, Professor Long Chen and Professor Hongkai Zhao for generously offering their time, support and valuable comments. In addition, I offer my thanks to Dr. Zhenlin Guo and Dr. Huaming Yan for helping me implement the numerical methods in Fortran.

CURRICULUM VITAE

Fei Yu

EDUCATION

Doctor of Philosophy in Mathematics **2013-2018**
University of California, Irvine *Irvine, CA*

Master's degree in Applied Mathematics **2011-2012**
North Carolina State University *Raleigh, NC*

Bachelor's degree in Computer System Engineering **2010-2011**
University of Birmingham *Birmingham, UK*

Bachelor's degree in Computer Science **2007-2011**
Harbin Institute of Technology *Harbin, China*

RESEARCH EXPERIENCE

Research Assistant **2014–2018**
University of California, Irvine *Irvine, California*

TEACHING EXPERIENCE

Teaching Assistant **2013–2018**
University of California, Irvine *Irvine, California*

Instructor **2017**
University of California, Irvine *Irvine, California*

PUBLICATIONS

Higher-Order Accurate Diffuse-Domain Methods for Partial Differential Equations with Dirichlet Boundary Conditions in Complex Geometries **2018**
In preparation

A Diffuse Domain Approach for Two Phase Flows with Large Density Ratio in Complex Geometries **2018**
In preparation

ABSTRACT OF THE DISSERTATION

Higher-Order Accurate Diffuse-Domain Methods for Partial Differential Equations with Dirichlet Boundary Conditions in Complex, Envolving Geometries

By

Fei Yu

Doctor of Philosophy in Mathematics

University of California, Irvine, 2018

Professor John Lowengrub, Chair

The diffuse-domain, or smoothed boundary, method is an attractive approach for solving partial differential equations in complex geometries because of its simplicity and flexibility. In this method the complex geometry is embedded into a larger, regular domain. The original PDE is reformulated using a smoothed characteristic function of the complex domain, here constructed from a level-set (signed distance) function, and source terms are introduced to approximate the boundary conditions. The reformulated equation can be solved by standard numerical methods and the same solver can be used for any domain geometry. A challenge is making the method higher order accurate. For Dirichlet boundary conditions, which we focus on here, current implementations demonstrate a wide range in their accuracy but generally the methods yield at best first order accuracy in ϵ, the parameter that characterizes the width of the region over which the characteristic function is smoothed. Typically, $\epsilon \propto h$, the grid size. Here, we analyze the diffuse-domain PDEs using matched asymptotic expansions and explain the observed behaviors. Our analysis also identifies simple modifications to the diffuse-domain PDEs that yield higher-order accuracy in ϵ, e.g., $O(\epsilon^2)$ in the L^2 norm and $O(\epsilon^p)$ with $1.5 \leq p \leq 2$ in the L^∞ norm. Our analytic results are confirmed numerically in stationary and moving domains. Finally, we extend our results to two-phase fluid problems and propose a diffuse domain approach to simulate two-phase flows in complex geometries.

Chapter 1

Introduction

1.1 Background

Many problems in the physical, biological and engineering sciences involve solving partial differential equations (PDEs) in complex geometries that change their size and shape in time. There are two main approaches for solving such problems. In one approach, interface-fitted meshes are used. Examples include finite element methods (e.g., [22]), boundary integral (e.g., [30]) and boundary element (e.g., [26]) methods. Because of the challenges associated with generating interface-fitted meshes for complex geometries, especially in three-dimensions, and because in many applications the complex geometry evolves in time, which would require a new mesh to be generated at each time step, embedded domain methods have been developed as an alternative approach.

In this second approach, the complex domain is embedded in a larger regular domain and the boundary conditions are approximated by a variety of different techniques. Examples include the adaptive fast multipole accelerated Poisson solver (e.g., [8]), which combines boundary and volume integral methods in the larger domain, fictitious domain methods (e.g.,

[34, 57, 31, 62]) where Lagrange multipliers are applied in order to enforce the boundary conditions, immersed boundary (e.g., [59, 24, 17, 75]), front-tracking (e.g., [78, 45, 74]) and arbitrary Lagrangian-Eulerian methods (e.g., [40, 9, 12, 48]) where force distributions supported in a neighborhood of the domain boundary are introduced to approximate the boundary conditions. In addition, immersed interface (e.g., [52, 43, 7, 54]), ghost fluid (e.g., [25, 50, 79, 32]), cut-cell methods (e.g., [44, 35, 61, 60]) and Voronoi interface (e.g., [72, 37]) methods modify difference stencils near the domain boundary to account for the boundary conditions. Further, the extended finite element method (e.g., [29, 10, 20]) approximates the boundary conditions by enriching the space of test functions. However, a disadvantage of most of these methods is that either modifications of standard finite element and finite difference software packages are needed or extra auxiliary equations have to be solved.

1.2 Diffuse-Domain Method

Diffuse-domain methods (DDM), also known as smoothed boundary methods, have emerged as an attractive alternative approach because they are easy to implement. No modifications of standard finite element or finite difference software are required and the same solver can be used for any domain geometry. In this approach the complex geometry is embedded into a larger, regular domain and a phase-field function is used to provide a smooth approximation to the characteristic function of the complex domain. In this thesis, we use a level-set method [64, 33] to generate the phase-field, or smoothed characteristic, function. A parameter ϵ, typically proportional to the grid size h, is introduced that characterizes the width of the transition region. The original PDE is reformulated with additional source terms that enforce the boundary conditions. While uniform meshes can be used, the DDM is most efficient when combined with adaptive mesh refinement to enable the use of small mesh sizes near the transition region and in regions of large gradients and large mesh sizes in the extended,

non-physical part of the regular domain.

Using rigorous mathematical theory [28, 1, 73, 16], matched asymptotic expansions and numerical simulations (e.g., [70, 53, 76, 81, 66]), the DDMs have been shown to converge to the original PDE and boundary conditions as the diffuse interface parameter ϵ tends to zero. Further, in [51] a matched asymptotic analysis for general DDMs with Neumann and Robin boundary conditions showed that for certain choices of the source terms, the DDMs were second-order accurate in ϵ and in the grid size h, taking $\epsilon \propto h$; see [16] for a rigorous proof.

For Dirichlet boundary conditions it is more challenging to obtain higher-order accurate diffuse domain methods. Current implementations of DDMs demonstrate a wide range in their accuracy but generally the methods yield at best first-order accuracy in ϵ [28, 81, 73, 16, 66]. For example, some schemes, including one presented in [53], achieve sub-first order accuracy $\mathcal{O}(\epsilon \ln \epsilon)$. While others, including some presented in [53, 81, 66], achieve first-order accuracy: $\mathcal{O}(\epsilon)$. Further, in [66] it was shown using asymptotic analysis that for several DDM approximations of the diffusion equation with Dirichlet boundary conditions, that while the order of accuracy was $\mathcal{O}(\epsilon)$ the error could be significantly reduced by special choices of the DDM parameters. However, because DDMs for Dirichlet boundary conditions derive from introducing penalty terms in the equation, which are inherently low-order accurate, new modifications must be introduced to achieve higher-order accuracy.

In Chapter 2 of this thesis, we analyze, using matched asymptotic expansions, several DDMs for approximating PDEs with Dirichlet boundary conditions. Our analysis explains the wide variation in the observed accuracy of the schemes and identifies simple modifications of the DDMs that can yield higher-order accuracy in ϵ. In particular, our new schemes are $\mathcal{O}(\epsilon^2)$ in the L^2 norm and $\mathcal{O}(\epsilon^p)$ in the L^∞ norm, with p ranging from 1.5 to 2 depending on the range of ϵ and h considered. For example, in the limit, $\epsilon \to 0$ and $\epsilon/h \to 0$ we obtain $p \to 1.5$. Interestingly, the schemes can be more accurate when $\epsilon \propto h$. The methods are dimension-

independent and easy to implement. Our analytic results are confirmed numerically in stationary and moving domains in $1D$ and $2D$. In the latter, we use finite-difference discretizations with a mass-conserving multigrid method on block-structured adaptive meshes [38] to obtain a highly-efficient scheme.

1.3 Applications of Diffuse-Domain Method

The diffuse-domain method was introduced in [49] to solve diffusion equations with Neumann (no-flux) boundary conditions using finite difference methods and later in [14, 15] using spectral methods. The DDM was extended to simulate PDEs on surfaces in [70], to PDEs with Robin and Dirichlet boundary conditions in [53] and to cases in which bulk and surface equations are coupled [76]. Later, in [81] and [66] alternate derivations of smoothed boundary methods for such problems were presented. Diffuse-domain methods have been applied to a wide variety of problems that arise, for example, in biology (e.g., [49, 27, 3, 18, 23, 69, 67, 56, 19]), in fluid dynamics (e.g., [77, 4, 5, 6, 2]) and in materials science (e.g., [82, 67, 68, 42, 21]).

In particular, many applications of multiphase flows involve complex flow domains, interfacial physics and the motion of contact lines separating immiscible components at solid boundaries. DDM has recently been coupled with two-phase fluid model to study the fluid flows in complex geometry [4]. However, the fluid model is restricted to the case where the density and viscosity of the two fluids have to be exactly the same. In Chapter 3 of this thesis, we extend their results and apply the diffuse domain approach to simulate binary flow with variable physical properties. We first present a thermodynamically consistent diffuse interface model, q-NSCH, for two phase flows with different density and viscosity. We then combine the diffuse-domain method with the q-NSCH model, namely the q-NSCH-DD model, to simulate two-phase flows in complex geometries. We find that the q-NSCH-DD model converges to the original q-NSCH model as the thickness of the diffuse domain inter-

face shrinks to 0.

The outline of the thesis is as follows. In Chapter 2, we analyze DDM approximations to the Poisson equation with Dirichlet boundary conditions and present 1D numerical results that confirm our analysis. We also extend our analysis and simulations to time-dependent equations on both stationary and moving domains, focusing on the heat equation with external forcing. Both 1D and 2D numerical simulations are presented. In Chapter 3, we consider a thermodynamically consistent diffuse interface model for two-phase flows with variable density and propose a DDM approximation to the model, namely q-NSCH-DD. Numerical simulations for two-phase fluid motions in complex geometries are provided. Finally, in Chapter 4, we present conclusions and discuss future work.

Chapter 2

Diffuse-Domain methods for Poisson and Heat Equations with Dirichlet Boundary Conditions in Complex Geometries

2.1 Diffuse domain method for the Poisson equation with Dirichlet boundary conditions

Consider the Poisson equation with Dirichlet boundary condition on a complex (non-regular) domain D:

$$\Delta u = f \quad in \quad D, \tag{2.1}$$

$$u = g \quad on \quad \partial D. \tag{2.2}$$

To approximate Eqs. (2.1) and (2.2), we present three DDM approximations defined in [53] and posed on a larger, regular domain Ω:

$$\textbf{DDM1}: \quad \nabla \cdot (\phi \nabla u_\epsilon) - \frac{1}{\epsilon^3}(1-\phi)(u_\epsilon - g) = \phi f, \tag{2.3}$$

$$\textbf{DDM2}: \quad \phi \Delta u_\epsilon - \frac{1}{\epsilon^2}(1-\phi)(u_\epsilon - g) = \phi f, \tag{2.4}$$

$$\textbf{DDM3}: \quad \nabla \cdot (\phi \nabla u_\epsilon) - \frac{|\nabla \phi|}{\epsilon^2}(u_\epsilon - g) = \phi f, \tag{2.5}$$

where the source terms $\frac{1}{\epsilon^3}(1-\phi)(u_\epsilon - g)$, $\frac{1}{\epsilon^2}(1-\phi)(u_\epsilon - g)$ and $\frac{|\nabla\phi|}{\epsilon^2}(u_\epsilon - g)$ represent different choices for enforcing the Dirichlet boundary condition $u = g$. The function ϕ approximates the characteristic function of D, e.g.

$$\phi(\boldsymbol{x}, t) = \frac{1}{2}(1 - \tanh(\frac{3r(\boldsymbol{x}, t)}{\epsilon})), \tag{2.6}$$

here ϵ is the interface thickness and $r(\boldsymbol{x}, t)$ is the signed-distance function to ∂D, which is taken to be negative inside D. Note that for DDM3, since the phase field function ϕ and its gradient vanish rapidly outside D, in order to prevent the equation from being ill-posed, we use the following modified $\hat{\phi}$ and its gradient instead in the numerical calculation [51],

$$\hat{\phi} = \tau + (1-\tau)\phi, \tag{2.7}$$

$$|\nabla \hat{\phi}| = \tau + (1-\tau)|\nabla \phi|, \tag{2.8}$$

where $\tau = 10^{-15}$. In all the DDMs we consider, we assume that the boundary function g is defined in a small $\mathcal{O}(\epsilon)$ neighborhood of ∂D using an extension off ∂D that is constant in the normal direction and that f is similarly extended smoothly out of the domain D.

2.1.1 Numerical results for DDM1-3

We present numerical results in 1D for the DDMs given in Sec. 2.1. We suppose the original Poisson equation is defined in $D = [-1.111, 1.111]$ with Dirichlet boundary conditions at $x = \pm 1.111$, which are not grid points. We take the forcing function $f = 1$ and boundary condition $g = 1.111^2/2$ so that the exact solution to Eqs. (2.1)-(2.2) is $u = x^2/2$. The results from other test cases can be found in Appendix B.

We solve the DDMs in a larger domain $\Omega = [-2, 2]$ with the same Dirichlet boundary condition as the original Poisson equation. Note that the choice for boundary condition for the outer domain Ω should not affect the inner domain D. Therefore the distance between ∂D and $\partial\Omega$ should be large compared to ϵ. The equations are discretized on a uniform grid with the standard second-order central difference scheme (adaptive mesh refinement is used later in 2D, see Sec. 2.3). The discrete system is solved using the Thomas method [41].

The numerical solutions of DDM1-3, together with the exact solution, are shown in Fig. 2.1(a), a close-up of the solutions with $x \in [-0.1, 0.1]$ is shown as an inset. Here, we have taken $\epsilon = 0.0125$ and $h = \epsilon/4$. We next calculate and compare the error between the simulated DDM solutions u_ϵ and the analytic solution u of the original PDE. We present the errors in both the L^2 and the L^∞ norms, defined as

$$E_\epsilon^{(2)} = \frac{\|\phi(u - u_\epsilon)\|_{L^2(\Omega)}}{\|\phi u\|_{L^2(\Omega)}}, \tag{2.9}$$

where $\|\cdot\|_{L^2}$ is the discrete L^2 norm:

$$\|u\|_{L^2} = \frac{\sqrt{\sum_{i=1}^N u_i^2}}{N}, \tag{2.10}$$

where N is the number of grid points in Ω. The error in the L^∞ norm is defined as [52]

$$E_\epsilon^{(\infty)} = \frac{\|(u - u_\epsilon)\|_{L^\infty(D)}}{\|u\|_{L^\infty(D)}}, \tag{2.11}$$

and $\|u\|_{L^\infty(D)} = \max_{1\le i\le M} |u_i|$ and M is the number of grid points in D . Note this is not L^∞ in Ω. The convergence rate in ϵ is calculated as

$$\boldsymbol{k} = \frac{\log(\frac{E_{\epsilon_i}}{E_{\epsilon_{i-1}}})}{\log(\frac{\epsilon_i}{\epsilon_{i-1}})}. \tag{2.12}$$

The results are presented in Tabs. 2.1 and 2.2. We observe that DDM2 is 1st order accurate, which is consistent with findings in [81, 66], while the convergence rates of DDM1 and DDM3 are less than 1 in both L^2 and L^∞ norms (see also Tabs. A.1-A.6 in Appendix B for other test cases).

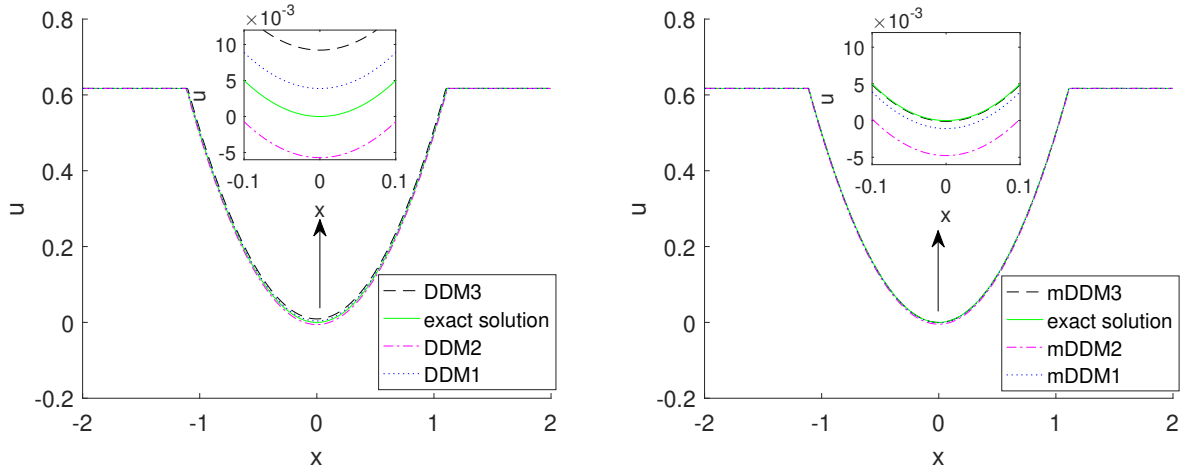

(a) (b)

Figure 2.1: (a). Numerical solutions of DDM1–3 from Eqs. (2.3)-(2.5); (b). The corresponding modified diffuse domain methods mDDM1-3 from Eqs. (2.78)-(2.80); with $f = 1$, $g = 1.111^2/2$, $\epsilon = 0.0125$ and $h = \epsilon/4$.

	DDM1				DDM3			
ϵ	$E^{(2)}$	$\boldsymbol{k}$	$E^{(\infty)}$	$\boldsymbol{k}$	$E^{(2)}$	$\boldsymbol{k}$	$E^{(\infty)}$	$\boldsymbol{k}$
2.00E-01	4.88E-01	0.00	2.12E-01	0.00	3.82E-02	0.00	4.73E-02	0.00
1.00E-01	1.12E-01	2.12	5.26E-02	2.01	9.45E-02	-1.31	4.42E-02	0.10
5.00E-02	9.88E-03	3.51	7.96E-03	2.72	8.03E-02	0.24	3.66E-02	0.27
2.50E-02	1.31E-02	-0.41	5.89E-03	0.44	5.39E-02	0.58	2.44E-02	0.59
1.25E-02	1.41E-02	-0.11	6.31E-03	-0.10	3.33E-02	0.69	1.50E-02	0.70
6.25E-03	1.04E-02	0.44	4.66E-03	0.44	1.97E-02	0.76	8.84E-03	0.76
3.13E-03	6.80E-03	0.62	3.04E-03	0.62	1.14E-02	0.79	5.09E-03	0.80
1.56E-03	4.16E-03	0.71	1.86E-03	0.71	6.42E-03	0.82	2.87E-03	0.82

Table 2.1: The L^2 and L^∞ errors in DDM1 and DDM3 with $h = \epsilon/4$.

	DDM2			
ϵ	$E^{(2)}$	$\boldsymbol{k}$	$E^{(\infty)}$	$\boldsymbol{k}$
2.00E-01	3.42E-01	0.00	1.65E-01	0.00
1.00E-01	1.70E-01	1.01	7.95E-02	1.05
5.00E-02	8.45E-02	1.01	3.88E-02	1.04
2.50E-02	4.17E-02	1.02	1.91E-02	1.02
1.25E-02	2.07E-02	1.01	9.51E-03	1.00
6.25E-03	1.03E-02	1.00	4.82E-03	0.98
3.13E-03	5.16E-03	1.00	2.40E-03	1.00
1.56E-03	2.58E-03	1.00	1.20E-03	1.01

Table 2.2: The L^2 and L^∞ errors in DDM2 with $h = \epsilon/4$.

To understand this behavior, the scaled errors near the boundary $x = 1.111$ are shown in Fig. 2.2. In Fig. 2.2(a), we plot $\frac{u_\epsilon - u}{\epsilon}$ versus the stretched inner variable $z = \frac{r}{\epsilon}$ ($r = x - 1.111$) using $\epsilon = 0.00625$ and $N = 2560$, which is obtained from the grid size $h = \frac{\epsilon}{4}$. When $z << 0$ (inside the domain), $\frac{u_\epsilon - u}{\epsilon}$ tends to a constant, $C(\epsilon)$. In Fig. 2.2(b), the constants $C(\epsilon)$ from DDM1 and DDM3 are plotted as a function of $\ln(\epsilon)$. Linear fits give that $C(\epsilon) \approx -0.186 \ln(\epsilon) - 0.475$ for DDM1 and $C(\epsilon) \approx -0.188 \ln(\epsilon) - 0.143$ for DDM3, which show that the orders of accuracy

of DDM1 and DDM3 are $\epsilon \ln(\epsilon)$ as $\epsilon \to 0$. In Fig. 2.2(c), we plot the limit value $C(\epsilon)$ from DDM2 as a function of ϵ. The plots suggest that $C(\epsilon) \to -0.45 \neq 0$, which implies DDM2 is 1st order accurate.

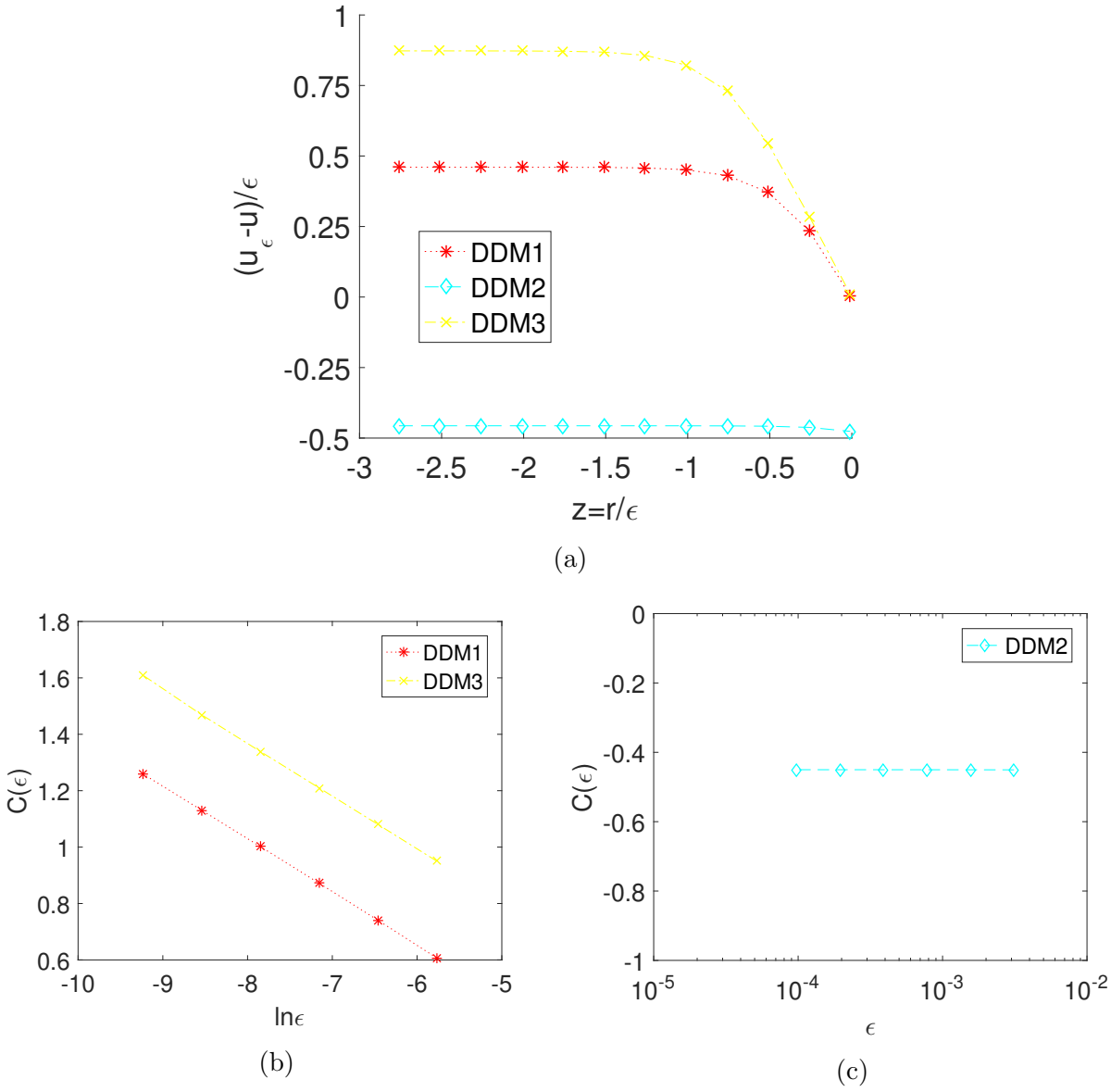

Figure 2.2: Comparisons of the behavior of DDM1, DDM2 and DDM3 near ∂D. (a): $\frac{u_\epsilon - u}{\epsilon}$ with $\epsilon = 0.00625$, (b): $C(\epsilon)$s for DDM1 and DDM3, (c): $C(\epsilon)$ for DDM2.

2.1.2 Matched asymptotic analysis of DDMs

In this section, we perform a matched asymptotic analysis in 1D for DDM1-3 in order to explain the numerical results in Sec. 2.1.1. This analysis can be easily extended to higher dimensions. Without loss of generality, we also assume the boundary is located at $x = 0$ and we take the signed distance (near the boundary) to be $r = x$, again $x < 0$ denotes the interior of D. We consider the expansion of diffuse-domain variables in powers of the interface thickness ϵ in regions close to and far from the interface, which are known as inner ($\hat{u}$) and outer ($\bar{u}$) expansions, respectively. On each side of the interface, there exists an outer expansion, here labeled $\bar{u}_1(x;\epsilon)$ where $x < 0$ and $\phi = 1$, and $\bar{u}_2(x;\epsilon)$ where $x > 0$ and $\phi = 0$. Clearly for all three DDMs, we have

$$\bar{u}_2 = g. \tag{2.13}$$

Note that there could be multiple layers near the boundary and hence multiple inner expansions may be required to match the two outer expansions.

2.1.2.1 Analysis of DDM2

We first present the matched asymptotic analysis of DDM2. In 1D, DDM2 is,

$$\phi \frac{d^2}{dx^2} u_\epsilon - \frac{1}{\epsilon^2}(1-\phi)(u_\epsilon - g) = \phi f, \tag{2.14}$$

We assume the outer expansion $\bar{u}_1$ satisfies,

$$\bar{u}_1(x;\epsilon) = \bar{u}_1^{(0)}(x) + \epsilon \bar{u}_1^{(1)}(x) + ... \tag{2.15}$$

Plugging into Eq. (2.14) and assuming that neither f nor g depends on ϵ, we have,

$$\frac{d^2}{dx^2}\bar{u}_1^{(0)} = f, \tag{2.16}$$

$$\frac{d^2}{dx^2}\bar{u}_1^{(k)} = 0, k = 1, 2, ... \tag{2.17}$$

Now, if $\bar{u}_1^{(0)} = g$ on ∂D so that $\bar{u}_1^{(0)}$ is the unique solution to Eqs. (2.1) and (2.2), then DDM2 reduces to the Poisson equation with Dirichlet boundary condition at leading order. The L^2 convergence rate is then determined by the next leading order term, $\bar{u}_1^{(1)}$. In order to determine $\bar{u}_1^{(0)}$ and $\bar{u}_1^{(1)}$, we need to analyze the behavior of DDM2 (Eq. (2.14)) near ∂D using inner expansions and then match the inner and outer expansions in a region of overlap.

To get the inner equations, we first derive the following simplified form of DDM2 by substituting ϕ with Eq. (2.6) and dividing by ϕ:

$$\frac{d^2}{dx^2}u_\epsilon - \frac{e^{6x/\epsilon}}{\epsilon^2}(u_\epsilon - g) = f. \tag{2.18}$$

Consider Eq. (2.18) in a region K_1, where $x \sim \mathcal{O}(\epsilon)$ and $e^{6x/\epsilon} \sim \mathcal{O}(1)$ and we introduce a stretched variable,

$$z_1 = \frac{x}{\epsilon}. \tag{2.19}$$

In a local coordinate system near ∂D, the derivatives become

$$\frac{d}{dx} = \frac{1}{\epsilon}\frac{d}{dz_1}, \tag{2.20}$$

$$\frac{d^2}{dx^2} = \frac{1}{\epsilon^2}\frac{d^2}{dz_1^2}, \tag{2.21}$$

The inner expansion associated with the stretched variable z_1 is

$$\hat{u}_1(z_1;\epsilon) = \hat{u}_1^{(0)}(z_1) + \epsilon\hat{u}_1^{(1)}(z_1) + ... \tag{2.22}$$

To obtain the matching conditions for each outer solution $\bar{u}_i$ $(i = 1, 2)$, we assume that there is a region of overlap where both the inner and the outer expansions are valid. In this region, if we evaluate the outer expansion in the inner coordinates, this must match the limits of the inner solutions away from the interface, that is,

$$\hat{u}_1(z_1;\epsilon) \simeq \bar{u}_1(\epsilon z_1;\epsilon), \text{ as } z_1 \to -\infty \text{ and } \epsilon z_1 \to 0^-, \tag{2.23}$$

$$\hat{u}_1(z_1;\epsilon) \simeq \bar{u}_2(\epsilon z_1;\epsilon) = g, \text{ as } z_1 \to +\infty \text{ and } \epsilon z_1 \to 0^+. \tag{2.24}$$

Here a single inner expansion $\hat{u}_1$ is able to match both outer expansions up to $\mathcal{O}(\epsilon)$ for DDM2 as shown below. As we see later in Sec. 2.1.2.2, this is not the case for DDM1 and DDM3 and an additional layer needs to be introduced. Combining Eqs. (2.13), (2.15), (2.22)-(2.24), we have the following asymptotic matching conditions up to $\mathcal{O}(\epsilon)$,

$$\hat{u}_1^{(0)}(z_1) = \bar{u}_1^{(0)}(0), \text{ as } z_1 \to -\infty, \tag{2.25}$$

$$\hat{u}_1^{(1)}(z_1) = \bar{u}_1^{(1)}(0) + z_1\frac{d}{dx}\bar{u}_1^{(0)}(0), \text{ as } z_1 \to -\infty, \tag{2.26}$$

and

$$\hat{u}_1^{(0)}(z_1) = g, \text{ as } z_1 \to +\infty, \tag{2.27}$$

$$\hat{u}_1^{(1)}(z_1) = 0, \text{ as } z_1 \to +\infty. \tag{2.28}$$

Plugging Eq. (2.22) into Eq. (2.18) and using derivatives in the local coordinate system

(Eqs. (2.20) and (2.21)), we obtain the following equations for the inner expansion $\hat{u}_1$:

$$\text{At } \mathcal{O}(\epsilon^{-2}), \qquad \frac{d^2}{dz_1^2}\hat{u}_1^{(0)} - e^{6z_1}(\hat{u}_1^{(0)} - g) = 0, \tag{2.29}$$

$$\text{At } \mathcal{O}(\epsilon^{-1}), \qquad \frac{d^2}{dz_1^2}\hat{u}_1^{(1)} - e^{6z_1}\hat{u}_1^{(1)} = 0. \tag{2.30}$$

The solution to the following homogeneous ordinary differential equation,

$$y'' - e^{6x}y = 0, \tag{2.31}$$

is given by

$$y = C_1 I_0(\frac{e^{3x}}{3}) + C_2 K_0(\frac{e^{3x}}{3}), \tag{2.32}$$

where I_0 and K_0 are the modified Bessel functions of the first and second kind, respectively, and C_1 and C_2 are constants. Clearly, $\hat{u}_1^{(0)} = g$ is a solution to Eq. (2.29). Therefore,

$$\hat{u}_1^{(0)}(z_1) = g + C_1 I_0(\frac{e^{3z_1}}{3}) + C_2 K_0(\frac{e^{3z_1}}{3}), \tag{2.33}$$

$$\hat{u}_1^{(1)}(z_1) = C_3 I_0(\frac{e^{3z_1}}{3}) + C_4 K_0(\frac{e^{3z_1}}{3}), \tag{2.34}$$

where C_i's are constants. The modified Bessel functions satisfy:

$$\lim_{z_1 \to -\infty} I_0(\frac{e^{3z_1}}{3}) = 1, \tag{2.35}$$

$$\lim_{z_1 \to +\infty} I_0(\frac{e^{3z_1}}{3}) = +\infty, \tag{2.36}$$

$$\lim_{z_1 \to -\infty} K_0(\frac{e^{3z_1}}{3}) \sim -\ln(\frac{1}{2}\frac{e^{3z_1}}{3}) - \gamma \sim -3z_1 + \ln 6 - \gamma, \tag{2.37}$$

$$\lim_{z_1 \to +\infty} K_0(\frac{e^{3z_1}}{3}) = 0, \tag{2.38}$$

where $\gamma \approx 0.5772$ is the Euler−Mascheroni constant. From Eq. (2.37) and the matching

condition (2.25) we conclude that $C_2 = 0$. Using Eq. (2.36) and the matching conditions as $z_1 \to +\infty$ (Eqs. (2.27) and (2.28)), we have $C_1 = C_3 = 0$. Putting everything together and using (2.26), we find

$$\hat{u}_1^{(0)} = g, \tag{2.39}$$

$$\hat{u}_1^{(1)} = -\frac{A}{3} K_0(\frac{e^{3z_1}}{3}) \sim A z_1 + \frac{A}{3}(-\ln 6 + \gamma), \text{ as } z_1 \to -\infty, \tag{2.40}$$

where $A = \frac{d}{dx}\bar{u}^{(0)}(0)$ is the derivative of the exact solution at the boundary. By the matching conditions (Eqs. (2.25) and (2.26)), the two leading terms of the outer solution $\bar{u}_1$ satisfies

$$\bar{u}_1^{(0)}(0) = g, \tag{2.41}$$

$$\bar{u}_1^{(1)}(0) = \frac{A}{3}(-\ln 6 + \gamma). \tag{2.42}$$

Therefore, $\bar{u}_1^{(0)} = u$, which is the exact solution of the Poisson equation with Dirichlet boundary condition (Eqs. (2.1) and (2.2)), and DDM2 is first order accurate in ϵ in the L^2 norm since $\bar{u}_1 - u \sim \mathcal{O}(\epsilon)$ if $A \neq 0$. As for the L^∞ norm, we also need to consider the error at the boundary , e.g., $\hat{u}_1(0) - g \approx \epsilon \hat{u}_1^{(1)}(0) \sim \mathcal{O}(\epsilon)$ for DDM2. Thus, DDM2 is first order accurate in ϵ in the L^∞ norm as well if $A \neq 0$. If $A = 0$, then the asymptotic analysis suggests better than first-order accuracy. In fact when $A = 0$, DDM2 is second-order accurate in both L^2 and L^∞ as shown in Appendix B.

To confirm our analysis, we compute $\bar{u}_1^{(1)}(0) \approx C(\epsilon)$, where $C(\epsilon) \approx (u_\epsilon - u)/\epsilon$ as $z_1 << 0$ is shown in Fig. 2.2(c). Using $A = 1.111$, both the asymptotic analysis and the numerical results agree and give $\bar{u}_1^{(1)} \approx -0.450$ (see Tab. C.1 in Appendix C for other cases).

2.1.2.2 Analysis of DDM1 and DDM3

We now extend the matched asymptotic analysis in Sec.2.1.2.1 to DDM1 and DDM3. In 1D, DDM1 reads,

$$\frac{d}{dx}(\phi\frac{d}{dx}u_\epsilon) - \frac{1}{\epsilon^3}(1-\phi)(u_\epsilon - g) = \phi f, \tag{2.43}$$

Substituting ϕ from Eq. (2.6), we have,

$$\frac{d^2}{dx^2}u_\epsilon - \frac{6}{\epsilon}\frac{1}{1+e^{-6x/\epsilon}}\frac{d}{dx}u_\epsilon - \frac{e^{6x/\epsilon}}{\epsilon^3}(u_\epsilon - g) = f. \tag{2.44}$$

We assume that

$$\bar{u}_1(x;\epsilon) = \bar{u}_1^{(0)}(x) + \epsilon\bar{u}_1^{(1)}(x;\ln\epsilon) + o(\epsilon). \tag{2.45}$$

Note that $\ln\epsilon$ is included in the outer expansion, which we will explain later. Plugging Eq. (2.45) into the DDM1 (Eq. (2.43)), again we have,

$$\frac{d^2}{dx^2}\bar{u}_1^{(0)} = f, \tag{2.46}$$

$$\frac{d^2}{dx^2}\bar{u}_1^{(k)} = 0, k = 1, 2, ... \tag{2.47}$$

As for inner expansion, we first consider DDM1 (Eq. (2.44)) in K_1, where $x \sim \mathcal{O}(\epsilon)$ and $e^{6x/\epsilon} \sim \mathcal{O}(1)$. We introduce the same stretched variable,

$$z_1 = \frac{x}{\epsilon}, \tag{2.48}$$

and the inner expansion,

$$\hat{u}_1(z_1;\epsilon) = \hat{u}_1^{(0)}(z_1) + \epsilon\hat{u}_1^{(1)}(z_1) + ..., \tag{2.49}$$

Plugging into Eq. (2.44), we have the following equations,

$$\text{At } \mathcal{O}(\epsilon^{-3}), \qquad e^{6z_1}(\hat{u}_1^{(0)} - g) = 0, \tag{2.50}$$

$$\text{At } \mathcal{O}(\epsilon^{-2}), \qquad \frac{d^2}{dz_1^2}\hat{u}_1^{(0)} - \frac{6}{1+e^{-6z_1}}\frac{d}{dz_1}\hat{u}_1^{(0)} - e^{6z_1}\hat{u}_1^{(1)} = 0, \tag{2.51}$$

$$\text{At } \mathcal{O}(\epsilon^{-1}), \qquad \frac{d^2}{dz_1^2}\hat{u}_1^{(1)} - \frac{6}{1+e^{-6z_1}}\frac{d}{dz_1}\hat{u}_1^{(1)} - e^{6z_1}\hat{u}_1^{(2)} = 0, \tag{2.52}$$

$$\text{At } \mathcal{O}(1), \qquad \frac{d^2}{dz_1^2}\hat{u}_1^{(2)} - \frac{6}{1+e^{-6z_1}}\frac{d}{dz_1}\hat{u}_1^{(2)} - e^{6z_1}\hat{u}_1^{(3)} = f, \tag{2.53}$$

$$\tag{2.54}$$

It follows that

$$\hat{u}_1^{(0)} = g, \tag{2.55}$$

$$\hat{u}_1^{(1)} = \hat{u}_1^{(2)} = 0, \tag{2.56}$$

$$\hat{u}_1^{(3)} = -fe^{-6z_1}. \tag{2.57}$$

Thus,

$$\hat{u}_1(z_1;\epsilon) = g - \epsilon^3 f e^{-6z_1} + o(\epsilon^3). \tag{2.58}$$

Clearly, $\hat{u}_1$ satisfies two of the matching conditions as $z_1 \to +\infty$ (Eqs. (2.27) and (2.28)). However, $\lim_{z_1\to-\infty} \hat{u}_1(z_1;\epsilon) = -\infty$, which implies $\hat{u}_1$ does not satisfy the other two matching conditions (Eqs. (2.25) and (2.26)) and hence there exists another layer, namely K_2 (and another inner solution, namely $\hat{u}_2$).

Accordingly, we introduce the layer K_2 where $x \sim \alpha\epsilon \ln(\epsilon) + \mathcal{O}(\epsilon)$. Here we choose $\alpha = 1/6$ and consider the two leading terms in the inner expansions, other choices of α will result different layers, but their inner expansions are the same up to $\mathcal{O}(\epsilon)$. We consider a new stretched variable,

$$z_2 = \frac{x - \epsilon(\ln \epsilon)/6}{\epsilon} = \frac{x}{\epsilon} - \frac{\ln \epsilon}{6} \tag{2.59}$$

Similar to Eq. (2.23), we derive the corresponding matching conditions in K_2, that is

$$\bar{u}_1(\epsilon z_2 + \frac{\epsilon \ln \epsilon}{6}) \simeq \hat{u}_2(z_2), \text{ as } z_2 \to -\infty \text{ and } \epsilon z_2 \to 0^-. \tag{2.60}$$

It follows that

$$\lim_{z_2 \to -\infty} \hat{u}_2^{(0)}(z_2) = \bar{u}_1^{(0)}(0), \tag{2.61}$$

$$\lim_{z_2 \to -\infty} \hat{u}_2^{(1)}(z_2) = \bar{u}_1^{(1)}(0) + (z_2 + \frac{\ln \epsilon}{6}) \frac{d}{dx} \bar{u}_1^{(0)}(0). \tag{2.62}$$

As $z_2 \to +\infty$, we need to match the inner solutions $\hat{u}_2(z_2)$ with $\hat{u}_1(z_1)$ from K_1. This is described below.

Plugging in the inner expansion into DDM1 (Eq. (2.44)) and using that $e^{6x/\epsilon} = \epsilon e^{6z_2}$, we obtain:

$$\text{At } \mathcal{O}(\epsilon^{-2}), \qquad \frac{d^2}{dz_2^2} \hat{u}_2^{(0)} - e^{6z_2}(\hat{u}_2^{(0)} - g) = 0, \tag{2.63}$$

$$\text{At } \mathcal{O}(\epsilon^{-1}), \qquad \frac{d^2}{dz_2^2} \hat{u}_2^{(1)} - 6e^{6z_2} \frac{d}{dz_2} \hat{u}_2^{(0)} - e^{6z_2} \hat{u}_2^{(1)} = 0. \tag{2.64}$$

The general solution to Eq. (2.63) is

$$\hat{u}_2^{(0)}(z_2) = g + C_1 I_0(\frac{e^{3z_2}}{3}) + C_2 K_0(\frac{e^{3z_2}}{3}), \tag{2.65}$$

where I_0 and K_0 are the modified Bessel functions of the first and second kind, respectively, and C_1, C_2 are constants.

Then we need to match $\hat{u}_2^{(0)}(z_2)$ with the leading order of the inner solution in K_1 (Eq. (2.55)) as $z_2 \to +\infty$, that is

$$\lim_{z_2 \to +\infty} \hat{u}_2^{(0)}(z_2) = g. \tag{2.66}$$

It follows that $C_1 = 0$. From Eq. (2.61) and (2.37), we obtain $C_2 = 0$. Thus,

$$\hat{u}_2^{(0)}(z_2) = g, \tag{2.67}$$

which implies

$$\bar{u}_1^{(0)}(0) = \lim_{z_2 \to -\infty} \hat{u}_2^{(0)}(z_2) = g. \tag{2.68}$$

Hence, DDM1 recovers the Poisson equation with Dirichlet boundary condition at leading order and $\bar{u}_1^{(0)}$ is the exact solution to Eqs. (2.1) and (2.2).

Plugging Eq. (2.67) into Eq. (2.64), we have

$$\hat{u}_2^{(1)}(z_2) = C_3 I_0(\frac{e^{3z_2}}{3}) + C_4 K_0(\frac{e^{3z_2}}{3}), \tag{2.69}$$

where C_3 and C_4 are constants. $\hat{u}_2^{(1)}$ needs to match $\hat{u}_1^{(1)} = 0$ in K_1 as $z_2 \to +\infty$, that is

$$\lim_{z_2 \to +\infty} \hat{u}_2^{(1)}(z_2) = 0, \tag{2.70}$$

Hence, $C_3 = 0$. On the other side where $z_2 \to -\infty$, by the matching condition Eq. (2.62),

we obtain

$$\lim_{z_2 \to -\infty} \hat{u}_2^{(1)}(z_2) = \bar{u}_1^{(1)}(0) + A(z_2 + \frac{\ln \epsilon}{6}), \tag{2.71}$$

where $A = \frac{d}{dx}\bar{u}_1^{(0)}(0)$ is the derivative of exact solution at the boundary $x = 0$. Therefore, taking the limit of Eq. (2.69) as $z_2 \to -\infty$ and equating the result to Eq. (2.71), it follows that

$$\bar{u}_1^{(1)}(0) = -\frac{A}{6}\ln \epsilon + \frac{A}{3}(-\ln 6 + \gamma) \sim \mathcal{O}(\ln \epsilon) \tag{2.72}$$

Hence, the convergence rate of DDM1 in the L^2 norm is $\epsilon \ln(\epsilon)$ if $A \neq 0$. Although the error at the boundary is $\hat{u}_1(0) - g \sim \mathcal{O}(\epsilon^3)$ as seen from Eq. (2.58)), the L^∞ error is dominated by $\epsilon \ln(\epsilon)$.

As for DDM3, Replacing $\frac{1-\phi}{\epsilon}$ with $\frac{|\nabla \phi|}{\epsilon^2}$ and conducting an analogous analysis, we obtain

$$\bar{u}_1^{(0)}(0) = g, \tag{2.73}$$

$$\bar{u}_1^{(1)}(0) = -\frac{A}{6}\ln \epsilon + \frac{A}{3}(-\ln(\frac{1}{2}\sqrt{\frac{2}{3}}) + \gamma) \sim \mathcal{O}(\ln \epsilon). \tag{2.74}$$

Thus, DDM3 is also of $\mathcal{O}(\epsilon \ln \epsilon)$ in both L^2 and L^∞ norms if $A \neq 0$. If $A = 0$, our analysis suggests that DDM1 and DDM3 are better than first-order accurate (see Appendix B).

To validate our analysis, we plot $C(\epsilon) \approx (u_\epsilon - u)/\epsilon$ versus $\ln(\epsilon)$ as in Fig. 2.2(b) and compute the slope through a linear fit using the numerical results in Sec. 2.1.1. For both DDM1 and DDM3, our asymptotic analysis suggests that the slope is $-A/6 \approx -0.185$ using $A = 1.111$. Numerically, we obtain the slopes -0.186 and -0.188 from DDM1 and DDM3, respectively, which agrees well with the theory (see Tab. C.2 in Appendix C for other cases).

2.1.3 Development and analysis of higher-order, modified DDMs

In order to achieve higher order accuracy, we need to guarantee that the first order term in the outer expansion ($\bar{u}_1$) vanishes, that is, $\bar{u}_1^{(1)} = 0$. From the matching condition, Eq. (2.26), we observe that if $\hat{u}_1^{(1)}(z_1)$ behaves as Az_1 as $z_1 \to -\infty$, where A is the derivative of the exact solution at the boundary, then $\bar{u}_1^{(1)}(0)$ must be 0 and hence $\bar{u}_1^{(1)}(x) = 0$ since $d^2\bar{u}_1^{(1)}/dx^2 = 0$ from Eqs. (2.17) and (2.47). Therefore, if we can modify the original DDMs in a way such the inner solution $\hat{u}_1(z_1)$ satisfies,

$$\lim_{z_1 \to \pm\infty} \hat{u}_1^{(0)}(z_1) = g, \tag{2.75}$$

$$\lim_{z_1 \to +\infty} \hat{u}_1^{(1)}(z_1) = 0, \tag{2.76}$$

$$\lim_{z_1 \to -\infty} \hat{u}_1^{(1)}(z_1) \sim Az_1, \tag{2.77}$$

we should be able to achieve higher-order accuracy based on the asymptotic analysis. Accordingly, this suggests that to achieve higher-order accuracy we may modify the DDMs (referred to as the mDDMs) in the following way:

$$\textbf{mDDM1}: \quad \nabla \cdot (\phi \nabla u_\epsilon) - \frac{1}{\epsilon^3}(1-\phi)(u_\epsilon - g - r\boldsymbol{n} \cdot \nabla u_\epsilon) = \phi f, \tag{2.78}$$

$$\textbf{mDDM2}: \quad \phi \Delta u_\epsilon - \frac{1}{\epsilon^2}(1-\phi)(u_\epsilon - g - r\boldsymbol{n} \cdot \nabla u_\epsilon) = \phi f, \tag{2.79}$$

$$\textbf{mDDM3}: \quad \nabla \cdot (\phi \nabla u_\epsilon) - \frac{|\nabla \phi|}{\epsilon^2}(u_\epsilon - g - r\boldsymbol{n} \cdot \nabla u_\epsilon) = \phi f, \tag{2.80}$$

where $\boldsymbol{n} = -\frac{\nabla \phi}{|\nabla \phi|}$ is the normal vector. Next, we analyze these methods in the following two sections to determine their actual order of accuracy.

2.1.3.1 Asymptotic analysis of mDDM1 and mDDM3

Similar to Sec. 2.1.2, we assume $x = 0$ is the boundary and $r = x$. Consider mDDM1 in 1D:

$$\frac{d}{dx}(\phi\frac{d}{dx}u_\epsilon) - \frac{1}{\epsilon^3}(1-\phi)(u_\epsilon - g - x\frac{d}{dx}u_\epsilon) = \phi f, \tag{2.81}$$

Substituting ϕ with Eq. (2.6), we obtain

$$\frac{d^2}{dx^2}u_\epsilon - \frac{6}{\epsilon}\frac{1}{1+e^{-6x/\epsilon}}\frac{d}{dx}u_\epsilon - \frac{e^{6x/\epsilon}}{\epsilon^3}(u_\epsilon - g - x\frac{d}{dx}u_\epsilon) = f. \tag{2.82}$$

After examining possible ways of performing matched asymptotic expansions for Eq. (2.82) and introducing multiple layers as in previous section, the simplest approach is to choose a new inner variable $z_3 = \frac{x}{\epsilon^{1.5}}$ and the corresponding inner solution $\hat{u}_3(z_3)$ in the region K_3, where $x \sim \epsilon^{1.5}$ and $e^{6x/\epsilon} \approx 1$. In the local coordinate system, the derivatives become

$$\frac{d}{dx} = \frac{1}{\epsilon^{1.5}}\frac{d}{dz_3}, \tag{2.83}$$

$$\frac{d^2}{dx^2} = \frac{1}{\epsilon^3}\frac{d^2}{dz_3^2}, \tag{2.84}$$

Similar to Eqs. (2.23) and (2.24), we develop matching conditions for K_3, that is,

$$\hat{u}_3(z_3;\epsilon) \simeq \bar{u}_1(\epsilon^{1.5}z_3;\epsilon), \text{ as } z_3 \to -\infty, \quad \text{and} \quad \epsilon^{1.5}z_3 \to 0^- \tag{2.85}$$

$$\hat{u}_3(z_3;\epsilon) \simeq \bar{u}_2(\epsilon^{1.5}z_3;\epsilon) = g, \text{ as } z_3 \to +\infty, \quad \text{and} \quad \epsilon^{1.5}z_3 \to 0^+. \tag{2.86}$$

Since we use the scale $\epsilon^{1.5}$, it is natural to include half powers in the outer and inner expan-

sions:

$$\bar{u}_1(x;\epsilon) = \bar{u}_1^{(0)}(x) + \epsilon^{0.5}\bar{u}_1^{(0.5)}(x) + \epsilon\bar{u}_1^{(1)}(x) + \epsilon^{1.5}\bar{u}_1^{(1.5)}(x)..., \tag{2.87}$$

$$\hat{u}_3(z_3;\epsilon) = \hat{u}_3^{(0)}(z_3) + \epsilon^{0.5}\hat{u}_3^{(0.5)}(z_3) + \epsilon\hat{u}_3^{(1)}(z_3) + \epsilon^{1.5}\hat{u}_3^{(1.5)}(z_3).... \tag{2.88}$$

Plugging into Eqs. (2.85) and (2.86), we obtain the matching conditions,

$$\hat{u}_3^{(0)}(z_3) = g, \text{ as } z_3 \to +\infty, \tag{2.89}$$

$$\hat{u}_3^{(k)}(z_3) = 0, k = 0.5, 1, 2, ..., \text{ as } z_3 \to +\infty, \tag{2.90}$$

and

$$\hat{u}_3^{(k)}(z_3) = \bar{u}_1^{(k)}(0), k = 0, 0.5, 1, \text{ as } z_3 \to -\infty, \tag{2.91}$$

$$\hat{u}_3^{(1.5)}(z_3) = \bar{u}_1^{(1.5)}(0) + z_3\frac{d}{dx}\bar{u}_1^{(0)}(0), \text{ as } z_3 \to -\infty. \tag{2.92}$$

Plugging Eq. (2.88) into Eq. (2.82) we derive the following inner equation at the leading order $\mathcal{O}(\epsilon^{-3})$:

$$\frac{d^2}{dz_3^2}\hat{u}_3^{(0)} - (\hat{u}_3^{(0)} - g - z_3\frac{d}{dz_3}\hat{u}_3^{(0)}) = 0, \tag{2.93}$$

Clearly, $\hat{u}_3^{(0)} = g$ is a solution to Eq. (2.93). The general solution to the following homogeneous ordinary differential equation,

$$y'' + xy' - y = 0, \tag{2.94}$$

involves a linear combination of parabolic cylinder functions ($D_{-2}(x)$) [11]:

$$y = e^{-x^2/4}(C_1 D_{-2}(x) + C_2 D_{-2}(-x)), \tag{2.95}$$

where C_1 and C_2 are constants. Thus,

$$\hat{u}_3^{(0)} = g + e^{-z_3^2/4}(C_1 D_{-2}(z_3) + C_2 D_{-2}(-z_3)), \tag{2.96}$$

where $D_{-2}(z_3) \sim z_3^2 e^{-z_3^2/4}$ as $z_3 \to +\infty$ and $D_{-2}(z_3) = -\sqrt{2\pi} z_3 e^{z_3^2/4}$ as $z_3 \to -\infty$. By the matching conditions (Eqs. (2.89) and (2.91)), we have

$$\hat{u}_3^{(0)} = g, \tag{2.97}$$

$$\bar{u}_1^{(0)}(0) = g. \tag{2.98}$$

Hence mDDM1 recovers the Poisson equation at the leading order, e.g., $\bar{u}_1^{(0)} = u$, the exact solution.

At the next order $\mathcal{O}(\epsilon^{-2.5})$ in Eq. (2.82), we have,

$$\frac{d^2}{dz_3^2}\hat{u}_3^{(0.5)} - (\hat{u}_3^{(0.5)} - z_3 \frac{d}{dz_3}\hat{u}_3^{(0.5)}) = 0. \tag{2.99}$$

Thus,

$$\hat{u}_3^{(0.5)} = e^{-z_3^2/4}(C_1 D_{-2}(z_3) + C_2 D_{-2}(-z_3)). \tag{2.100}$$

Again, using the matching conditions (Eqs. (2.90) and (2.91)), we derive $\hat{u}_3^{(0.5)} = 0$. A similar argument at $\mathcal{O}(\epsilon^{-2})$ in Eq. (2.82) gives $\hat{u}_3^{(1)} = 0$.

At $\mathcal{O}(\epsilon^{-1.5})$ in Eq. (2.82), we obtain,

$$\frac{d^2}{dz_3^2}\hat{u}_3^{(1.5)} - (\hat{u}_3^{(1.5)} - z_3 \frac{d}{dz_3}\hat{u}_3^{(1.5)}) = 0. \tag{2.101}$$

Hence,

$$\hat{u}_3^{(1.5)} = e^{-z_3^2/4}(C_1 D_{-2}(z_3) + C_2 D_{-2}(-z_3)). \tag{2.102}$$

Applying the matching conditions (Eqs. (2.90) and (2.92)), we get

$$\hat{u}_3^{(1.5)} = -\frac{Ae^{-z_3^2/4}}{\sqrt{2\pi}} D_{-2}(z_3) \sim Az_3 \text{ as } z_3 \to -\infty, \tag{2.103}$$

where $A = \frac{d}{dx}\bar{u}_1^{(0)}(0)$ is the derivative of the exact solution at the boundary. Plugging into Eq. (2.92), we conclude

$$\bar{u}_1^{(1.5)}(0) = 0. \tag{2.104}$$

Thus, the asymptotic analysis suggests that $\bar{u}_1(x) = \bar{u}_1^{(0)}(x) + \mathcal{O}(\epsilon^2)$ and mDDM1 is 2nd order accurate in ϵ in the L^2 norm as desired.

To analyze the error in the L^∞ norm, we need to consider the error at the boundary. At the boundary, $\hat{u}_3(0) - g \sim \epsilon^{1.5}\hat{u}_3^{(1.5)}(0) = -\frac{A\epsilon^{1.5}}{\sqrt{2\pi}}$. This suggests that mDDM1 is 1.5 order accurate in ϵ in the L^∞ norm.

This analysis can be easily extended to higher dimensions and to mDDM3 to obtain the same conclusions. The only difference with respect to mDDM3 is that $\frac{1-\phi}{\epsilon^3}$ is replaced with $\frac{|\nabla\phi|}{\epsilon^2}$, which gives $\hat{u}_3(0) - g \sim \epsilon^{1.5}\hat{u}_3^{(1.5)}(0) = -\frac{A\epsilon^{1.5}}{\sqrt{6\pi}}$. The errors in the L^2 norm and L^∞ norm are still suggested to be 2nd and 1.5 orders, respectively.

To confirm our analysis, we compute $\hat{u}_3^{(1.5)}(0)$ numerically in the following way. We plot the values of $(u_\epsilon - u)/\epsilon^{1.5}$ at the boundary ($z_3 = 0$) versus $\sqrt{\epsilon}$, where u_ϵ is the numerical solution, and we find the y-intercept of a quadratic fit. Since $A = 1.111$, our asymptotic analysis gives that the values of $\hat{u}_3^{(1.5)}(0)$ are -0.443 and -0.256 for mDDM1 and mDDM3, respectively. We obtain -0.442 and -0.257 from the numerical results of mDDM1 and mDDM3, respectively,

which is consistent with our theory (see Tab. C.3 in Appendix C for other cases).

2.1.3.2 Asymptotic analysis of mDDM2

Even though mDDM2 is obtained using the same modification as in mDDM1 and mDDM3, surpisingly as our analysis below suggests and numerical results confirm (see Sec. 2.1.4), mDDM2 is only first-order accurate in both L^2 and L^∞. In 1D, the mDDM2 is:

$$\phi \frac{d^2}{dx^2} u_\epsilon - \frac{1}{\epsilon^2}(1-\phi)(u_\epsilon - g - x\frac{d}{dx}u_\epsilon) = \phi f. \tag{2.105}$$

Substituting ϕ from Eq. (2.6), we obtain

$$\frac{d^2}{dx^2} u_\epsilon - \frac{e^{6x/\epsilon}}{\epsilon^2}(u_\epsilon - g - x\frac{d}{dx}u_\epsilon) = f. \tag{2.106}$$

Considering Eq. (2.106) in K_1, we use the inner variable $z_1 = \frac{x}{\epsilon}$ to derive the following inner equations for $\hat{u}_1$:

$$\text{At } \mathcal{O}(\epsilon^{-2}), \qquad \frac{d^2}{dz_1^2}\hat{u}_1^{(0)} - e^{6z_1}(\hat{u}_1^{(0)} - g - z_1\frac{d}{dz_1}\hat{u}_1^{(0)}) = 0, \tag{2.107}$$

$$\text{At } \mathcal{O}(\epsilon^{-1}), \qquad \frac{d^2}{dz_1^2}\hat{u}_1^{(1)} - e^{6z_1}(\hat{u}_1^{(1)} - z_1\frac{d}{dz_1}\hat{u}_1^{(1)}) = 0. \tag{2.108}$$

Clearly, $\hat{u}_1^{(0)} = g$ is a solution to Eq. (2.107), and the general solution to the homogeneous ordinary differential equation below,

$$y'' - e^{6x}(y - xy') = 0, \tag{2.109}$$

is given by,

$$y = C_1 x + C_2(-e^{e^{6x}(1-6x)/36} - x\int_0^x h(t)dt), \tag{2.110}$$

where $h(x) = e^{e^{6x}(1-6x)/36+6x}$ (see Appendix D for details). It follows that

$$\hat{u}_1^0(z_1) = g + C_1 z_1 + C_2(-e^{e^{6z_1}(1-6z_1)/36} - z_1 \int_0^{z_1} h(t)dt), \tag{2.111}$$

$$\hat{u}_1^1(z_1) = C_3 z_1 + C_4(-e^{e^{6z_1}(1-6z_1)/36} - z_1 \int_0^{z_1} h(t)dt), \tag{2.112}$$

where the C_i are constants and

$$\lim_{z_1 \to -\infty} e^{e^{6z_1}(1-6z_1)/36} = 1, \tag{2.113}$$

$$\lim_{z_1 \to +\infty} e^{e^{6z_1}(1-6z_1)/36} = 0, \tag{2.114}$$

$$\lim_{z_1 \to -\infty} \int_0^{z_1} h(t)dt \approx 0.17, \tag{2.115}$$

$$\lim_{z_1 \to +\infty} \int_0^{z_1} h(t)dt \approx 2.75. \tag{2.116}$$

Combining with the matching conditions as $z_1 \to \pm\infty$ (Eqs. (2.25)-(2.28)) and solving for the constants C_i, we obtain that

$$\hat{u}_1^{(0)}(z_1) = g, \tag{2.117}$$

$$\hat{u}_1^{(1)}(z_1) \approx \frac{A}{2.92}(-e^{e^{6z_1}(1-6z_1)/36} + z_1 \int_{z_1}^{\infty} h(t)dt), \tag{2.118}$$

where as before A is the derivative of the exact solution at the boundary. Therefore,

$$\lim_{z_1 \to -\infty} \hat{u}^{(1)}(z_1) \sim A z_1 - \frac{A}{2.92}, \tag{2.119}$$

which implies

$$\bar{u}_1^{(1)}(0) \approx -\frac{A}{2.92} \neq 0, \text{ if } A \neq 0. \tag{2.120}$$

This suggests mDDM2 is 1st order accurate in ϵ in the L^2 norm when $A \neq 0$. Plugging $z_1 = 0$ into Eq. (2.118) and we have

$$\hat{u}_1^{(1)}(0) \approx -\frac{Ae^{1/36}}{2.92}, \tag{2.121}$$

which implies that mDDM2 is also 1st order accurate in the L^∞ norm.

To confirm our analysis, we compute $\bar{u}_1^{(1)}$ numerically, which is given by $(u_\epsilon - u)/\epsilon$ as $z << 0$, using the numerical solution u_ϵ in Sec. 2.1.4. In addition, we interpolate and plot the boundary values of $(u_\epsilon - u)/\epsilon$ at $z_1 = 0$ versus ϵ, and then calculate $\hat{u}^{(1)}(0)$ from the y-intercept of a linear fit. Since $A = 1.111$, our analysis indicates that $\bar{u}_1^{(1)} \approx -\frac{A}{2.92} \approx -0.381$ and $\hat{u}^{(1)}(0) \approx -\frac{Ae^{1/36}}{2.92} \approx -0.391$. The numerical results suggest that $\bar{u}_1^{(1)} \approx -0.380$ and $\hat{u}^{(1)}(0) \approx -0.391$, which agrees very well with the theory (see Tab. C.4 in Appendix C for other cases).

2.1.4 Numerical results for mDDM1-3

We adopt the same problem setup and an analogous discretization as in Sec. 2.1.1. The results using $h = \epsilon/4$ are presented in Fig. 2.1(b). Clearly mDDM3 and mDDM1 are more accurate than DDM1-3 and mDDM2. Further, mDDM2 and DDM2 (Fig. 2.1(a)) display similar levels of accuracy as suggested by our analysis.

To test the order of accuracy in ϵ predicted by theory, we take $h = \epsilon^{1.5}/4$ in order to resolve the inner layer K_3, as guided by our asymptotic analysis in Sec. 2.1.3.1. Later, in Secs. 2.2 and 2.3, we will test convergence with $\epsilon \propto h$. In Tabs. 2.3 and 2.4, we present convergence results for mDDM1-3 for case 1 (see also Tabs. B.1-B.6 in Appendix A for other cases). Consistent with our analysis, we observe that mDDM1 and mDDM3 are approximately 2nd order accurate in the L^2 norm but approximately 1.5 order accurate in the L^∞ norm. Also

as predicted, mDDM2 is only 1st order accurate in both norms. Therefore, we recommend using mDDM1 or mDDM3.

In practice, taking $h \sim \epsilon^{1.5}$ is too constraining for solving problems in 2D and 3D. Instead, one may choose $h = \epsilon/c$. Doing this, one can obtain results with orders of accuracy ranging from 1.5 to 2 (1.5 for large c and approximately 2 for $c \approx 4$; see Tabs. 2.5-2.9 in Secs. 2.2 and 2.3).

	mDDM1				mDDM3			
ϵ	$E^{(2)}$	$\boldsymbol{k}$	$E^{(\infty)}$	$\boldsymbol{k}$	$E^{(2)}$	$\boldsymbol{k}$	$E^{(\infty)}$	$\boldsymbol{k}$
2.00E-01	4.88E-01	0.00	2.10E-01	0.00	1.55E-01	0.00	8.23E-02	0.00
1.00E-01	1.50E-01	1.70	6.59E-02	1.67	3.77E-02	2.04	2.23E-02	1.88
5.00E-02	4.46E-02	1.75	1.98E-02	1.74	8.54E-03	2.14	5.96E-03	1.91
2.50E-02	1.26E-02	1.83	5.58E-03	1.83	1.89E-03	2.17	2.03E-03	1.55
1.25E-02	3.34E-03	1.91	1.55E-03	1.85	4.16E-04	2.19	6.15E-04	1.72
6.25E-03	8.61E-04	1.95	4.91E-04	1.65	8.74E-05	2.25	2.29E-04	1.42

Table 2.3: The L^2 and L^∞ errors for mDDM1 and mDDM3 with $h = \epsilon^{1.5}/4$.

	mDDM2			
ϵ	$E^{(2)}$	$\boldsymbol{k}$	$E^{(\infty)}$	$\boldsymbol{k}$
2.00E-01	4.58E-01	0.00	2.19E-01	0.00
1.00E-01	2.24E-01	1.03	1.06E-01	1.05
5.00E-02	1.11E-01	1.02	5.19E-02	1.03
2.50E-02	5.47E-02	1.02	2.59E-02	1.00
1.25E-02	2.72E-02	1.01	1.29E-02	1.01
6.25E-03	1.36E-02	1.00	6.45E-03	1.00

Table 2.4: The L^2 and L^∞ errors for mDDM2 with $h = \epsilon^{1.5}/4$.

2.2 Time-dependent problems

We next extend the mDDMs to simulate time-dependent PDEs in a moving domain $D(t)$ with Dirichlet boundary conditions. As we discuss later, our approach and analysis holds for much more general time-dependent equations, but we consider the diffusion equation here for simplicity of presentation:

$$\partial_t u = \Delta u + f \text{ in } D(t), \tag{2.122}$$

$$u = g \text{ on } \partial D(t). \tag{2.123}$$

2.2.1 Derivation and analysis of high-order, modified DDMs for time-dependent PDEs

To approximate Eq. (2.122), we formulate the diffuse domain model using an approximation (mDDMt3), which is analogous to mDDM3 in Sec. 2.1.3.1:

$$\textbf{mDDMt3:} \quad \partial_t(\phi u_\epsilon) = \nabla(\phi \nabla u_\epsilon) - \frac{1}{\epsilon^2}|\nabla\phi|(u_\epsilon - g - r\boldsymbol{n}\cdot\nabla u_\epsilon) + \phi f, \tag{2.124}$$

where as before r is the signed distance function, with $r < 0$ denoting the interior of D. Since the domain may be time-dependent, ϕ may depend on time and thus ϕ needs to be in the time derivative [53].

The asymptotic analysis for the time-dependent problem is very similar to that for the Poisson equation presented in Sec. 2.1.3.1. The only difference is that now the time derivative must be analyzed as well. Assuming the inner and outer expansions and matching conditions hold as in Sec. 2.1.3.1, from the leading order outer equation, we find that $\bar{u}_1^{(0)}$ satisfies Eq. (2.122).

In the inner expansion, taking $z_3 = x/\epsilon^{1.5}$, the time derivative can be written as:

$$\partial_t = -\frac{v}{\epsilon^{1.5}}\partial_{z_3} + o(1) \tag{2.125}$$

where v is the normal velocity of the domain boundary. Since ∂_t is of order $\epsilon^{-1.5}$, the time derivative will not affect the higher-order terms in the inner expansions of mDDM3. Therefore, we can still derive $\hat{u}_3^{(0)} = g$ and $\hat{u}_3^{(0.5)} = \hat{u}_3^{(1)} = 0$. Plugging into the inner equation at the next leading order ($\mathcal{O}(\epsilon^{-1.5})$), we obtain the same solution for $\hat{u}_3^{(1.5)}$ as that for the time-independent equation. Thus, mDDMt3 should be 1.5 order accurate in ϵ for the time-dependent (diffusion) equation. Similarly, the analogous time-dependent versions of mDDM1 and mDDM2 should also be 1.5 order and 1st order accurate in ϵ, respectively (results not shown).

2.2.2 Numerical results using mDDMt3 for time-dependent problems

For time-dependent problems, we first assume the domain does not change in time. Then, taking $f = \cos(x)\cos(t) + \cos(x)\sin(t)$ and $g = \cos(1.111)\sin(t)$, we obtain the exact solution $u = \cos(x)\sin(t)$ on the domain D=[-1.111,1.111]. We use central difference discretizations in space (as in Sec. 2.1.1) and the Crank-Nicholson method discretization in time to solve Eq. (2.124) on the larger domain $\Omega = [-2, 2]$ with ϕ from Eq. (2.6). We still use the Thomas algorithm to solve the tridiagonal matrix system. We calculate the errors at $t = 1$ in the L^2 and L^∞ norms by setting $dt = h$ where dt and h are the time step and grid size, respectively. Here, instead of taking $h \propto \epsilon^{1.5}$ as in the previous section, we instead take $h = \epsilon/c$ where c is a constant.

Various choices of c have been tested and here we present results using $c = 4, 16, 128$ in Tabs.

2.5, 2.6. We observe that mDDMt3 is 2nd order accurate in the L^2 norm for all choices of c. However, in L^∞, we find that when $c = 4$, the schemes are roughly 2nd order accurate in ϵ while if $c = 128$ the order of accuracy decreases to 1.5, consistent with our theory. In Fig. 2.3, we show the numerical solutions of mDDMt3 near the boundary $x = 1.111$ for difference choices of c. When $c = 4$, the boundary layer K_3 is not resolved and hence the numerical solution is less smooth near the boundary than is the continuous solution of mDDMt3. Nevertheless, it is actually closer to the exact solution close to the boundary of D. As the K_3 boundary layer is resolved by taking successively larger values of c, the solution is smoother and consequently deviates more near the boundary from the exact solution, which eventually results in errors that scale like $\mathcal{O}(\epsilon^{1.5})$ in L^∞ as predicted by theory. Outside of D, the mDDMt3 solutions tend to the extension of the exact solution, that is constant in the normal direction, because the boundary condition at $\partial\Omega$ is equal to the boundary condition at ∂D. Other choices of boundary conditions at $\partial\Omega$ would yield similar errors near ∂D but different behavior far from D (results not shown).

ϵ	c=4	**k**	c=16	**k**	c=128	**k**
0.2	2.85E-02	0.00	2.88E-02	0.00	0.028771	0.00
0.1	7.18E-03	1.99	7.37E-03	1.97	0.0073714	1.96
0.05	1.68E-03	2.10	1.75E-03	2.08	0.0017524	2.07
0.025	4.06E-04	2.05	4.17E-04	2.07	0.00041831	2.07
0.0125	9.66E-05	2.07	1.02E-04	2.03	0.00010247	2.03
0.00625	2.46E-05	1.98	2.58E-05	1.99	0.00002586	1.99

Table 2.5: The L^2 errors for simulating the time-dependent (diffusion) equation using mDDMt3 with $h = \epsilon/c$ on a fixed domain.

ϵ	c=4	**k**	c=16	**k**	c=128	**k**
0.2	3.87E-02	0.00	3.85E-02	0.00	4.01E-02	0.00
0.1	9.99E-03	1.95	1.09E-02	1.82	1.17E-02	1.77
0.05	2.15E-03	2.22	3.09E-03	1.82	3.45E-03	1.77
0.025	4.99E-04	2.11	1.04E-03	1.57	1.06E-03	1.70
0.0125	1.57E-04	1.67	3.17E-04	1.72	3.30E-04	1.69
0.00625	4.34E-05	1.85	8.64E-05	1.87	1.12E-04	1.56

Table 2.6: The L^∞ errors for simulating the time-dependent (diffusion) equation using mDDMt3 with $h = \epsilon/c$ on a fixed domain.

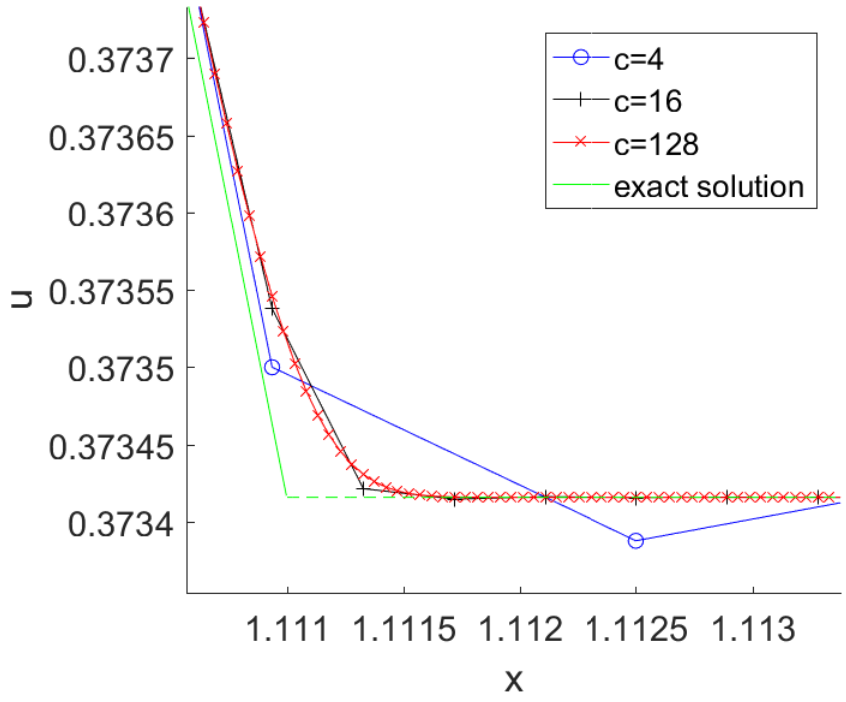

Figure 2.3: Numerical solutions of mDDMt3 near the boundary $x = 1.111$ on the 1D stationary domain with different c. The green dashed line denotes the extension (e.g., constant in the normal direction) of the exact solution out of the domain.

Next we assume the boundary of the domain is also moving and set $x_l(t) = -1.111$, $x_r(t) = 1.111 + 0.5t$, where $x_l(t)$ and $x_r(t)$ represent the left and right hand sides of the domain D,

respectively. We take $f = \cos(x)\cos(t) + \cos(x)\sin(t)$, $g = \cos(x_*)\sin(t)$, where $x_* = x_l, x_r$, and the exact solution $u = \cos(x)\sin(t)$.

In general, neither the signed distance function r nor the function ϕ are given analytically. Because we need to use the signed distance function in the modified DDMs, we find it convenient to apply the level-set method [64, 33] to determine both r and ϕ. Therefore, we solve the following Hamilton-Jacobi equation:

$$\partial_t r + v|\nabla r| = 0, \tag{2.126}$$

using a 5th order upwind WENO scheme [46] and a 2nd order Total Variation Diminishing (TVD) Runge-Kutta (RK) method time discretization to obtain an accurate fully discrete solution [36]. In order to keep $|\nabla r| = 1$, we periodically perform reinitialization [58, 71] by solving the following equation,

$$\partial_\tau r = \mathrm{sgn}_h(r^0)(1 - |\nabla r|), \tag{2.127}$$

where τ is pseudo time and $\mathrm{sgn}_h(r^0)$ is a smoothed approximation function of the sign of the initial signed distance function [65]:

$$\mathrm{sgn}_h(r) = \begin{cases} -1 & r < -h \\ 1 & r > h \\ \frac{r}{h} + \frac{1}{\pi}\sin(\frac{\pi r}{h}) & \text{else} \end{cases}$$

To determine whether reinitialization is needed or not, we calculate the slope of r near the boundaries of $D(t)$. Then we check if the maximum difference between the absolute value of the slope and 1 exceeds a threshold, here taken to be 0.01. If so, then we perform reinitialization.

Once the signed distance function $r(x,t)$ is obtained, we construct the phase field function

ϕ through Eq. (2.6). Next, we solve mDDMt3 using the same numerical setup as before and present the errors at $t = 1$ in the L^2 and L^∞ norms in Tabs. 2.7 and 2.8. The results are very similar to the stationary domain case. We again find that mDDMt3 is 2nd order accurate in the L^2 norm and between 1.5 and 2nd order accurate in the L^∞ norm, which is consistent with our analysis.

ϵ	c = 4	**k**	c = 16	**k**	c = 128	**k**
0.2	3.07E-02	0.00	3.07E-02	0.00	3.07E-02	0.00
0.1	7.91E-03	1.95	8.04E-03	1.93	8.05E-03	1.93
0.05	1.90E-03	2.06	1.95E-03	2.04	1.95E-03	2.04
0.025	4.73E-04	2.00	4.78E-04	2.03	4.79E-04	2.03
0.0125	1.18E-04	2.00	1.21E-04	1.99	1.21E-04	1.98
0.00625	2.97E-05	1.99	3.12E-05	1.95	3.15E-05	1.94

Table 2.7: The L^2 errors for simulating the time-dependent (diffusion) equation using mDDMt3 with $h = \epsilon/c$ on a moving domain.

ϵ	c = 4	**k**	c = 16	**k**	c = 128	**k**
0.2	4.38E-02	0.00	4.35E-02	0.00	4.51E-02	0.00
0.1	1.16E-02	1.92	1.25E-02	1.80	1.35E-02	1.75
0.05	2.57E-03	2.17	3.62E-03	1.79	4.06E-03	1.73
0.025	6.36E-04	2.01	1.23E-03	1.56	1.26E-03	1.68
0.0125	2.02E-04	1.66	3.74E-04	1.72	3.98E-04	1.67
0.00625	5.04E-05	2.00	1.02E-04	1.87	1.35E-04	1.55

Table 2.8: The L^∞ errors for simulating the time-dependent (diffusion) equation using mDDMt3 with $h = \epsilon/c$ on a moving domain.

2.3 2D numerical results

Now we consider the 2D diffusion equation Eqs. (2.122) and (2.123) on a moving 2D domain $D(t)$. The initial domain is enclosed by the polar curve (shown in Fig. 2.5(a)):

$$r(\theta) = 1 + 0.1\cos(3\theta) + 0.02\cos(5\theta). \tag{2.128}$$

We suppose the velocity of the domain $\boldsymbol{v}(\boldsymbol{x}, t)$ is given by,

$$\boldsymbol{v} = (0.2(1+2t)\cos(3\theta) + 0.12(1+6t)\cos(5\theta))(\cos(\theta), \sin(\theta)), \tag{2.129}$$

and solve for the signed distance function $r(x,t)$ using the level-set method as described in Sec. 2.2.2. The phase field function ϕ is determined from the signed distance function r via Eq. (2.6). We choose f and g such that the exact solution is $u(r,\theta,t) = \frac{1}{4}r^2$. The initial condition is $u_0(r,\theta) = \frac{1}{4}r^2$. We solve mDDMt3 (Eq. (2.124)) on the larger domain $\Omega = [-2,2] \times [-2,2]$ using the Crank-Nicholson method and the standard second-order central difference scheme together with adaptive, block-structured mesh refinement [80]. The implicit equations are solved using a mass-conserving multigrid solver [38]. The L^2 and L^∞ norms of the errors are calculated using 2D extensions of Eqs. (2.9) and (2.11). We use an adaptive mesh with a maximum of three levels of refinement. The mesh is refined according to the undivided gradient of $(u_\epsilon \phi)$, e.g., if $|\nabla (u_\epsilon \phi)| \geq 10^{-4}/(2h)$, where h is the local grid size, then the mesh is targeted for block-structured refinement (see [80] for details). We start with $\epsilon = 0.2$ and the coarse mesh grid size $h_{coarse} = 4/16$, which gives the fine mesh size $h_{fine} = 4/128 = \frac{5}{32}\epsilon$, and the time step $dt = 0.1/128$. Then, the parameters ϵ, h_{coarse} and dt are refined at the same time while the number of levels and $h_{fine} = \epsilon/6.4$ are fixed.

Note that for the 2D numerical numerical implementation, we need to discretize $\boldsymbol{n}$ in the following way in order for the solver to converge:

$$\boldsymbol{n} = \begin{cases} -\frac{\nabla\phi}{|\nabla\phi|} & \text{in } D, \\ 0 & \text{else.} \end{cases}$$

The solution u_ϵ in the evolving domain is shown at $t = 0.1$ using $\epsilon = 0.025$ in Fig. 2.4(a). In Figs. 2.4(b), 2.4(c) and Tab. 2.9, the L^2 and L^∞ errors are shown at this time. The results suggest mDDMt3 is 2nd order accurate in h, ϵ and dt in L^2 and between 1.5 and 2nd order in L^∞, consistent with our theory and numerical results from the previous section.

In Fig. 2.5, we present a long time simulation of the dynamics using mDDMt3 (Eq. (2.124)) with $\epsilon = 0.025$, $h_{coarse} = 4/64$, three levels of mesh refinement and $dt = 0.1/512$. We present the solution restricted to the moving domain $D(t)$ at different times, up to t=1.9. The point-wise error at $t = 1.9$ is shown in Fig. 2.5(f) and the largest error, which is of order 10^{-3}, occurs near the right most finger. As can be seen from these figures, mDDMt3 is able to accurately simulate solutions on time-dependent, highly complex non-rectangular domains.

In the next section, we apply DDM2 to a thermodynamically consistent diffuse interface model (q-NSCH) to simulate two-phase flows in complex geometries.

ϵ	L^2 **error**	**k**	L^∞ **error**	**k**
0.2	8.89E-02	0.00	1.01E-01	0.00
0.1	2.18E-02	2.03	2.91E-02	1.80
0.05	4.91E-03	2.15	8.35E-03	1.80
0.025	1.13E-03	2.12	2.37E-03	1.82
0.0125	2.90E-04	1.96	6.78E-04	1.81

Table 2.9: The L^2 and L^∞ errors for simulating the 2D time-dependent diffusion equation at t=0.1 using mDDMt3 on the moving domain $D(t)$.

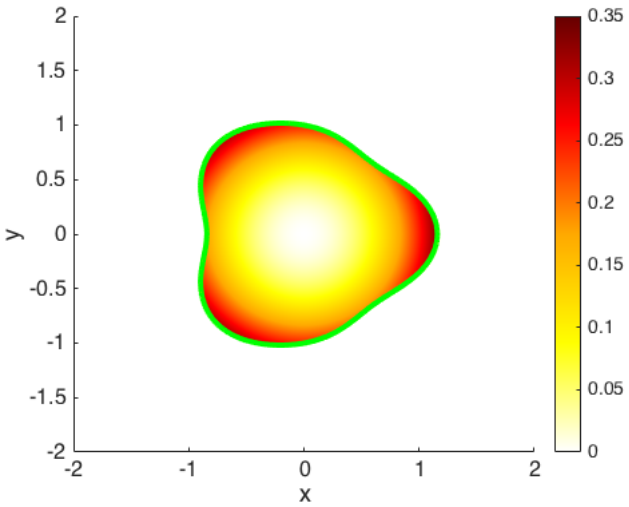

(a)

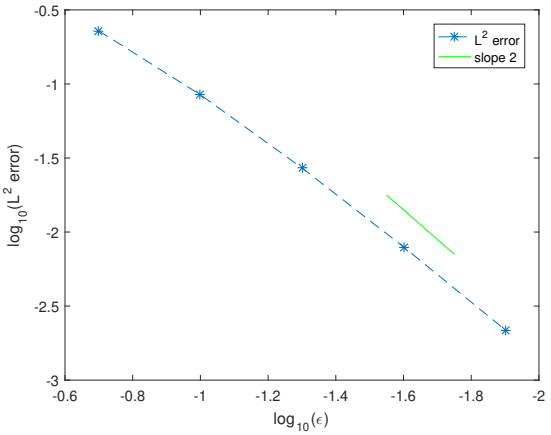

(b)

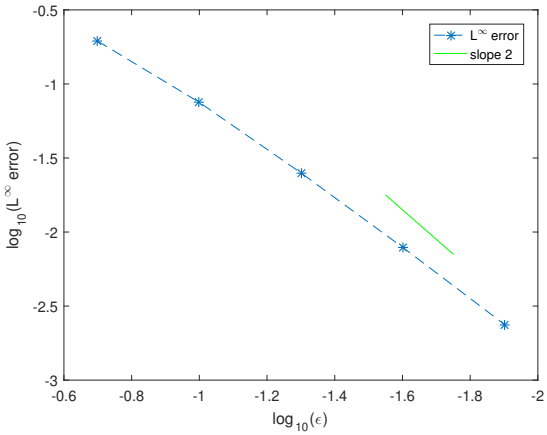

(c)

Figure 2.4: Error analysis of the 2D diffusion equation using mDDMt3 on the moving domain $D(t)$, see text for details. The green curve denotes the boundary ∂D. (a): The solution at $t = 0.1$ restricted on $D(t)$ with the boundary contour (green line), (b): The L^2 error at t=0.1, (c): The L^∞ error at t=0.1.

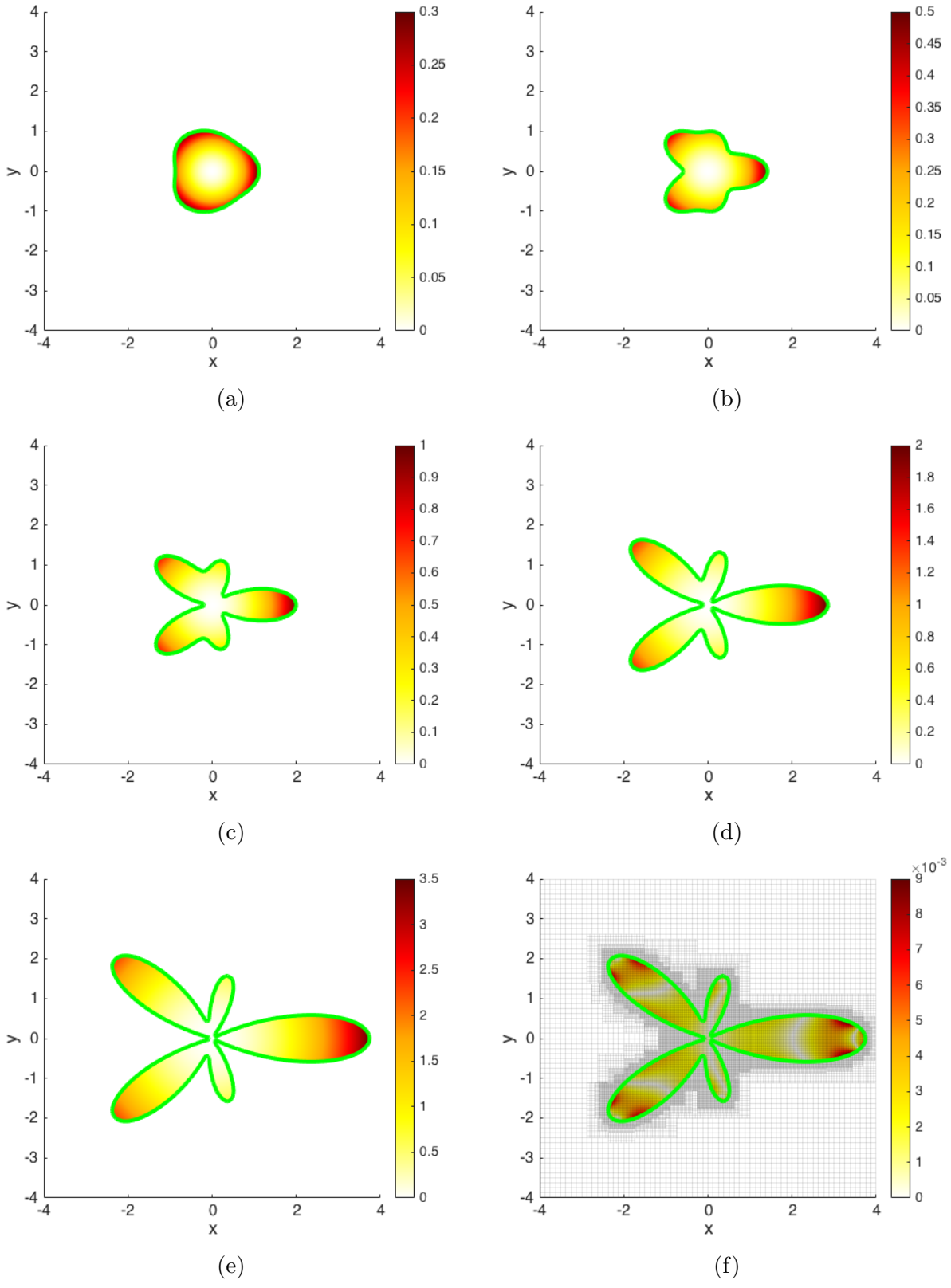

Figure 2.5: Solution of mDDMt3 from Eq. (2.124) at different times. The solution is restricted to $D(t)$ whose boundary ∂D is denoted by the green curve. See text for details. (a): t=0, (b): t=0.5, (c): t=1.0, (d): t=1.5, (e): t=1.9. (f): The point-wise error at t=1.9.

Chapter 3

Diffuse-Domain Methods for Simulating Two-Phase Flows in Complex Domains

3.1 q-NSCH model

In [39], a thermodynamically consistent diffuse interface model is presented to simulate two-phase flows with variable density and viscosity. Considering a two-phase fluid in a domain D, the model equations are given by

$$\rho \boldsymbol{u}_t + \rho \boldsymbol{u} \cdot \boldsymbol{\nabla} \boldsymbol{u} = -\boldsymbol{\nabla} p + \boldsymbol{\nabla} \cdot (\nu \boldsymbol{\nabla} \boldsymbol{u}) + \frac{1}{3} \boldsymbol{\nabla} (\nu \boldsymbol{\nabla} \cdot \boldsymbol{u}) + \frac{\sigma}{\epsilon_c} \mu \boldsymbol{\nabla} c + \rho g \boldsymbol{z}, \tag{3.1}$$

$$\boldsymbol{\nabla} \cdot \boldsymbol{u} = \alpha \boldsymbol{\nabla} \cdot (M(c) \boldsymbol{\nabla} \mu) + \alpha^2 \boldsymbol{\nabla} \cdot (M(c) \boldsymbol{\nabla} p), \tag{3.2}$$

$$c_t + \boldsymbol{u} \cdot \boldsymbol{\nabla} c = \boldsymbol{\nabla} \cdot \big(M(c) \boldsymbol{\nabla} \mu \big) + \alpha \boldsymbol{\nabla} \cdot (M(c) \boldsymbol{\nabla} p), \tag{3.3}$$

$$\mu = \epsilon_c F'(c) - \epsilon_c^2 \Delta c, \tag{3.4}$$

where $\boldsymbol{u}$ is the velocity, p the pressure, c the phase field variable, μ the chemical potential, g the gravitational constant, and $\boldsymbol{z}$ the unit vector in vertical direction. The variable density ρ and viscosity μ are defined as

$$\rho(c) = \rho_1 c + \rho_2(1-c), \quad \nu(c) = \nu_1 c + \nu_2(1-c), \tag{3.5}$$

where ρ_i and ν_i are constants for the ith fluid ($i = 1, 2$), and $\alpha = (\rho_2 - \rho_1)/\rho_2$. The function $F(c) = c^2(c-1)^2/4\epsilon_c$ is the double well potential, where ϵ_c is a small parameter that characterizes the interface thickness, $M(c) = \sqrt{c^2 \times (c-1)^2 + \delta}$ is the mobility function with a small parameter δ, and σ is the surface tension, which is related to the physical surface tension $\tilde{\sigma}$ through $\tilde{\sigma} = 3\sigma/\sqrt{2}$. The following boundary conditions on $\partial\Omega$ are imposed:

$$\boldsymbol{u} = \boldsymbol{u}_g, \quad \text{(no slip)}, \tag{3.6}$$

$$\boldsymbol{n} \cdot \boldsymbol{\nabla}(\mu + \alpha p) = 0, \quad \text{(no flux)}, \tag{3.7}$$

$$\boldsymbol{n} \cdot \boldsymbol{\nabla} c = \frac{1}{\epsilon_c \sqrt{2}} \cos(\theta)(1-c)c, \quad \text{(contact angle)}. \tag{3.8}$$

Here $\boldsymbol{u}_g = (g_u, g_v)$ is the velocity on the boundary $\partial\Omega$ and $\boldsymbol{n}$ is the outward normal vector to D. Assuming ∂D is closed, the boundary velocity needs to satisfy $\int_{\partial\Omega} \boldsymbol{u}_g \cdot \boldsymbol{n} \, \mathrm{d}S = 0$. θ is the static contact angle between the fluid-fluid interface and the physical boundary [47].

3.2 Diffuse domain reformulation: q-NSCH-DD

Now we assume the domain D is non-standard. To solve the q-NSCH model Eqs. (3.1)-(3.4) numerically, we extend the results in [4] and use DDM2 in Chapter 2 to propose a diffuse

domain approximation in a larger, regular domain Ω, namely q-NSCH-DD:

$$\rho(\phi \boldsymbol{u})_t + \rho \boldsymbol{u} \cdot \boldsymbol{\nabla}(\phi \boldsymbol{u}) = -\phi \boldsymbol{\nabla} p + \phi \boldsymbol{\nabla} \cdot (\nu \boldsymbol{\nabla} \boldsymbol{u}) + \frac{\phi}{3} \boldsymbol{\nabla}(\nu \boldsymbol{\nabla} \cdot \boldsymbol{u}) + \frac{\sigma}{\epsilon_c} \phi \mu \boldsymbol{\nabla} c + \phi \rho g \boldsymbol{z} + BC_{\boldsymbol{u}}, \tag{3.9}$$

$$\boldsymbol{\nabla} \cdot (\phi \boldsymbol{u}) = \boldsymbol{u}_g \cdot \boldsymbol{\nabla} \phi + \alpha \boldsymbol{\nabla} \cdot (M(c) \phi \boldsymbol{\nabla} \mu) + \alpha^2 \boldsymbol{\nabla} \cdot (M(c) \phi \boldsymbol{\nabla} p) + BC_{\mu,p}, \tag{3.10}$$

$$(\phi c)_t + \boldsymbol{u} \cdot \boldsymbol{\nabla}(\phi c) = \boldsymbol{\nabla} \cdot \big(\phi M(c) \boldsymbol{\nabla} \mu\big) + \alpha \boldsymbol{\nabla} \cdot (M(c) \phi \boldsymbol{\nabla} p) + BC_{\mu,p}, \tag{3.11}$$

$$\phi \mu = \phi \epsilon_c F'(c) - \epsilon_c^2 \boldsymbol{\nabla} \cdot (\phi \boldsymbol{\nabla} c) + BC_c, \tag{3.12}$$

with the boundary conditions $\boldsymbol{u} = \boldsymbol{u}_g$, $\boldsymbol{n} \cdot \boldsymbol{\nabla} c = \boldsymbol{n} \cdot \boldsymbol{\nabla} \mu = \boldsymbol{n} \cdot \nabla p = 0$ on $\partial\Omega$. Here the diffuse domain function ϕ, given by Eq. (2.6), is used to approximate the characteristic function of the original domain D. $r(\boldsymbol{x}, t)$ is the signed distance to ∂D and ϵ is the thickness of the diffuse domain interface. The reformulated BC_* are used to enforce the original boundary conditions (3.6)-(3.8) on ∂D. In particular,

$$BC_{\boldsymbol{u}} = -\frac{1-\phi}{\epsilon^2}(\boldsymbol{u} - \boldsymbol{u}_g), \tag{3.13}$$

$$BC_{\mu,p} = 0, \tag{3.14}$$

$$BC_c = -\frac{\epsilon_c |\nabla \phi|}{\sqrt{2}} \cos(\theta)(1-c)c \text{ [51]}. \tag{3.15}$$

In the next section, we show that the q-NSCH-DD system (3.9)-(3.12) converges to the original q-NSCH system (3.1)-(3.4) with B.C. (3.6)-(3.8), as $\epsilon \to 0$, using similar asymptotic analysis as in Chapter 2.

3.3 Asymptotic analysis of q-NSCH-DD

Now we consider the dimension-independent expansion of diffuse-domain variables in powers of the interface thickness ϵ in regions close to and far from the boundary $\partial\Omega$, which are known as inner ($\hat{Y}$) and outer expansions ($\bar{Y}$), respectively. Y represents $\boldsymbol{u}$, c, μ or p. Here we assume $\epsilon << \epsilon_c$. The two expansions are then matched in a region where both are valid.

3.3.1 Outer expansions

On each side of the interface, there exists an outer expansion, here labelled $\bar{Y}_1(x;\epsilon)$ where $r < 0$ and $\phi = 1$, and $\bar{Y}_2(x;\epsilon)$ where $r > 0$ and $\phi = 0$, where $\bar{Y}_i$ represents $\bar{\boldsymbol{u}}_i$, $\bar{c}_i$, $\bar{\mu}_i$ or $\bar{p}_i$. Clearly, $\bar{\boldsymbol{u}}_2 = \boldsymbol{u}_g$ and $\boldsymbol{n}\cdot\nabla\bar{p}_2 = \boldsymbol{n}\cdot\nabla\bar{\mu}_2 = \boldsymbol{n}\cdot\nabla\bar{c}_2 = 0$. We assume the outer solution Y_1 satisfy

$$\bar{Y}_1(\boldsymbol{x};\epsilon) = \bar{Y}_1^{(0)}(\boldsymbol{x}) + \epsilon\bar{Y}_1^{(1)}(\boldsymbol{x}) + ..., i = 1, 2 \tag{3.16}$$

Plugging into Eqs. (3.9)-(3.12), we obtain

$$\rho\frac{\partial}{\partial_t}\bar{\boldsymbol{u}}_1^{(0)} + \rho\bar{\boldsymbol{u}}_1^{(0)}\cdot\boldsymbol{\nabla}\bar{\boldsymbol{u}}_1^{(0)} = -\boldsymbol{\nabla}\bar{p}_1^{(0)} + \boldsymbol{\nabla}\cdot(\nu\boldsymbol{\nabla}\bar{\boldsymbol{u}}_1^{(0)}) + \frac{1}{3}\boldsymbol{\nabla}(\nu\boldsymbol{\nabla}\cdot\bar{\boldsymbol{u}}_1^{(0)}) + \frac{\sigma}{\epsilon_c}\bar{\mu}_1^{(0)}\boldsymbol{\nabla}\bar{c}_1^{(0)} + \rho g\boldsymbol{z}, \tag{3.17}$$

$$\boldsymbol{\nabla}\cdot\bar{\boldsymbol{u}}_1^{(0)} = \alpha\boldsymbol{\nabla}\cdot(M(\bar{c}_1^{(0)})\boldsymbol{\nabla}\bar{\mu}_1^{(0)}) + \alpha^2\boldsymbol{\nabla}\cdot(M(\bar{c}_1^{(0)})\boldsymbol{\nabla}\bar{p}_1^{(0)}), \tag{3.18}$$

$$\frac{\partial}{\partial_t}\bar{c}_1^{(0)} + \bar{\boldsymbol{u}}_1^{(0)}\cdot\boldsymbol{\nabla}\bar{c}_1^{(0)} = \boldsymbol{\nabla}\cdot\left(M(\bar{c}_1^{(0)})\boldsymbol{\nabla}\bar{\mu}_1^{(0)}\right) + \alpha\boldsymbol{\nabla}\cdot\left(M(\bar{c}_1^{(0)})\boldsymbol{\nabla}\bar{p}_1^{(0)}\right), \tag{3.19}$$

$$\bar{\mu}_1^{(0)} = \epsilon_c F'(\bar{c}_1^{(0)}) - \epsilon_c^2\boldsymbol{\nabla}\cdot(\boldsymbol{\nabla}\bar{c}_1^{(0)}), \tag{3.20}$$

Now, if $\bar{\boldsymbol{u}}_1^{(0)}$, $\bar{p}_1^{(0)}$, $\bar{\mu}_1^{(0)}$ and $\bar{c}_1^{(0)}$ satisfy the corresponding boundary conditions on $\partial\Omega$ so that they are the unique solutions to q-NSCH (3.1)-(3.4), then the q-NSCH-DD system recovers

the q-NSCH model at the leading order.

3.3.2 Inner expansions

As for the inner expansions, we introduce a local coordinate system near the interface $\partial\Omega$,

$$\boldsymbol{x}(\boldsymbol{s}, z; \epsilon) = \boldsymbol{X}(\boldsymbol{s}; \epsilon) + \epsilon z \boldsymbol{n}(\boldsymbol{s}; \epsilon), \tag{3.21}$$

where $\boldsymbol{X}(\boldsymbol{s}; \epsilon)$ is a parametrization of the interface, $\boldsymbol{n}(\boldsymbol{s}; \epsilon)$ is the interface normal vector that points out of Ω, z is the stretched variable,

$$z = \frac{r(\boldsymbol{x})}{\epsilon},$$

and $r(\boldsymbol{x})$ is the signed distance function to $\partial\Omega$. Note that $\lim_{z\to-\infty} \phi = 1$ and $\lim_{z\to+\infty} \phi = 0$. In the local coordinate system, the derivatives become

$$\boldsymbol{\nabla} = \frac{1}{\epsilon}\boldsymbol{n}\partial_z + \frac{1}{1+\epsilon z\kappa}\boldsymbol{\nabla}_s, \tag{3.22}$$

$$\Delta = \frac{1}{\epsilon^2}\partial_{zz} + \frac{1}{\epsilon}\frac{\kappa}{1+\epsilon z\kappa}\partial_z + \frac{1}{1+\epsilon z\kappa}\boldsymbol{\nabla}_s \cdot (\frac{1}{1+\epsilon z\kappa}\boldsymbol{\nabla}_s), \tag{3.23}$$

$$\partial_t = -\frac{\boldsymbol{n}\cdot\boldsymbol{u}}{\epsilon}\partial_z + o(1), \tag{3.24}$$

where $\kappa = \boldsymbol{\nabla}_{\boldsymbol{s}} \cdot \boldsymbol{n}$ is the surface curvature. We assume that the inner expansion is given by

$$\hat{Y}(z, \boldsymbol{s}; \epsilon) = \hat{Y}^{(0)}(z, \boldsymbol{s}) + \epsilon\hat{Y}^{(1)}(z, \boldsymbol{s}) + ..., \tag{3.25}$$

where $\hat{Y}$ represents $\hat{\boldsymbol{u}}$, $\hat{c}$, $\hat{\mu}$ and $\hat{p}$. In the region of overlap, we have

$$\bar{Y}_1(\boldsymbol{X} + \epsilon z \boldsymbol{n}; \epsilon) \simeq \hat{Y}(z, \boldsymbol{s}; \epsilon), \text{ as } z \to -\infty \tag{3.26}$$

$$\bar{Y}_2(\boldsymbol{X} + \epsilon z \boldsymbol{n}; \epsilon) \simeq \hat{Y}(z, \boldsymbol{s}; \epsilon), \text{ as } z \to +\infty. \tag{3.27}$$

Combining Eqs. (3.16), (3.25), (3.26) and (3.27), we have the following asymptotic matching conditions at the first two leading orders,

$$\lim_{z \to -\infty} \hat{Y}^{(0)}(z, \boldsymbol{s}) = \bar{Y}_1^{(0)}(\boldsymbol{s}), \tag{3.28}$$

$$\lim_{z \to -\infty} \hat{Y}^{(1)}(z, \boldsymbol{s}) = \bar{Y}_1^{(1)}(\boldsymbol{s}) + z\boldsymbol{n} \cdot \nabla \bar{Y}_1^{(0)}, \tag{3.29}$$

$$\lim_{z \to +\infty} \hat{Y}^{(0)}(z, \boldsymbol{s}) = \bar{Y}_2^{(0)}(\boldsymbol{s}), \tag{3.30}$$

$$\lim_{z \to +\infty} \hat{Y}^{(1)}(z, \boldsymbol{s}) = \bar{Y}_2^{(1)}(\boldsymbol{s}) + z\boldsymbol{n} \cdot \nabla \bar{Y}_2^{(0)}. \tag{3.31}$$

Plugging the inner expansions into q-NSCH-DD and using the local derivatives, we derive the following inner equations at the leading order $\mathcal{O}(\epsilon^{-2})$:

$$\text{Eq. (3.9)} \implies \frac{4}{3}\phi(\nu(\hat{\boldsymbol{u}}^{(0)} \cdot \boldsymbol{n})_z)_z - (1-\phi)(\hat{\boldsymbol{u}}^{(0)} - \boldsymbol{u}_g) \cdot \boldsymbol{n} = 0, \tag{3.32}$$

$$\text{Eq. (3.9)} \implies \phi(\nu(\hat{\boldsymbol{u}}^{(0)} \cdot \boldsymbol{s})_z)_z - (1-\phi)(\hat{\boldsymbol{u}}^{(0)} - \boldsymbol{u}_g) \cdot \boldsymbol{s} = 0, \tag{3.33}$$

$$\text{Eq. (3.10)} \implies \alpha\big(M(\hat{c}^{(0)})\phi(\hat{\mu}^{(0)} + \alpha\hat{p}^{(0)})_z\big)_z = 0, \tag{3.34}$$

$$\text{Eq. (3.11)} \implies \big(M(\hat{c}^{(0)})\phi(\hat{\mu}^{(0)} + \alpha\hat{p}^{(0)})_z\big)_z = 0, \tag{3.35}$$

$$\text{Eq. (3.12)} \implies -\epsilon^2(\phi\hat{c}_z^{(0)})_z = 0, \tag{3.36}$$

Here we assume $\nu = 1$ for simplicity and obtain

$$\hat{\boldsymbol{u}}^{(0)} \cdot \boldsymbol{n} = \boldsymbol{u}_g \cdot \boldsymbol{n} + C_1 I_0(\frac{e^{3z}}{2\sqrt{3}}) + C_2 K_0(\frac{e^{3z}}{2\sqrt{3}}), \tag{3.37}$$

$$\hat{\boldsymbol{u}}^{(0)} \cdot \boldsymbol{s} = \boldsymbol{u}_g \cdot \boldsymbol{s} + C_3 I_0(\frac{e^{3z}}{3}) + C_4 K_0(\frac{e^{3z}}{3}), \tag{3.38}$$

$$(\hat{\mu}^{(0)} + \alpha\hat{p}^{(0)})_z = 0, \tag{3.39}$$

$$\hat{c}^{(0)} = C_5, \tag{3.40}$$

where C_* are constants. I_0 and K_0 are the modified Bessel functions of the first and second kinds, respectively, which satisfy Eqs. (2.35)-(2.38). Combining Eqs. (3.37) and (3.38) with the leading order matching conditions for $\boldsymbol{u}$ (Eqs. (3.28) and (3.30)), we derive $\bar{\boldsymbol{u}}_1^{(0)} = \hat{\boldsymbol{u}}^{(0)} = \boldsymbol{u}_g$. At the next order of Eqs. (3.10) - (3.12), we obtain

$$\begin{aligned}(\phi \boldsymbol{n} \cdot \hat{\boldsymbol{u}}^{(0)})_z - \boldsymbol{u}_g \cdot \boldsymbol{n}\phi_z = 0 = {} & \alpha\big(M(\hat{c}^{(0)})\phi(\hat{\mu}^{(1)} + \alpha\hat{p}^{(1)})_z\big)_z \\ & + \alpha\big(M(\hat{c}^{(1)})\phi(\hat{\mu}^{(0)} + \alpha\hat{p}^{(0)})_z\big)_z,\end{aligned} \tag{3.41}$$

$$\big(\phi M(\hat{c}^{(0)})(\hat{\mu}^{(1)} + \alpha\hat{p}^{(1)})_z\big)_z = -\hat{\boldsymbol{u}}^{(0)} \cdot \boldsymbol{n}(\phi\hat{c}^{(0)})_z + \hat{\boldsymbol{u}}^{(0)} \cdot \boldsymbol{n}(\phi\hat{c}^{(0)})_z = 0, \tag{3.42}$$

$$(\phi\hat{c}_z^{(1)})_z = -\frac{\phi_z}{\epsilon_c\sqrt{2}}\cos(\theta))\,(1 - C_5)\,C_5. \tag{3.43}$$

Integrating Eqs. (3.42) and (3.43) both sides from $-\infty$ to $+\infty$ with respect to z, we have

$$\lim_{z\to-\infty}(\hat{\mu}^{(1)} + \alpha\hat{p}^{(1)})_z = 0, \tag{3.44}$$

$$\lim_{z\to-\infty}\hat{c}_z^{(1)} = \frac{1}{\epsilon\sqrt{2}}\cos(\theta)\,(1 - C_5)\,C_5. \tag{3.45}$$

Using the matching condition (Eq. (3.29)), we obtain

$$\boldsymbol{n} \cdot \boldsymbol{\nabla}(\bar{\mu}_1^{(0)} + \alpha\bar{p}_1^{(0)}) = 0, \tag{3.46}$$

$$\boldsymbol{n} \cdot \boldsymbol{\nabla}\bar{c}_1^{(0)} = \frac{1}{\epsilon\sqrt{2}}\cos(\theta)\,(1 - C_5)\,C_5. \tag{3.47}$$

Therefore, the outer solutions $\bar{\boldsymbol{u}}_1^{(0)}$, $\bar{\mu}_1^{(0)}$, $\bar{p}_1^{(0)}$ and $\bar{c}_1^{(0)}$ satisfy the original boundary conditions Eqs. (3.6)-(3.8). Hence the q-NSCH-DD system recovers the q-NSCH model at the leading order.

3.4 Numerical method and implementation

We now present a projection method for the q-NSCH-DD system (3.9)-(3.12) in the time-discrete level. Let dt denote the time step, and assume, $\boldsymbol{u}^n$, p^n, c^n and μ^n are the solutions at time $t = ndt$. We then find that the solutions at time $t = (n+1)dt$, namely $\boldsymbol{u}^{n+1}$, p^{n+1}, c^{n+1} and μ^{n+1}, satisfy:

$$\frac{\phi^{n+1}\rho^{n+1}\tilde{\boldsymbol{u}}^{n+1} - \phi^n\rho^n\boldsymbol{u}^n}{dt} + \phi^n\rho^n\boldsymbol{u}^n\cdot\boldsymbol{\nabla}\boldsymbol{u}^n = \phi^{n+1}\boldsymbol{\nabla}\cdot\left(\nu^n\boldsymbol{\nabla}\tilde{\boldsymbol{u}}^{n+1}\right) + \frac{\phi^{n+1}}{3}\nabla\left(\nu^n\boldsymbol{\nabla}\cdot\tilde{\boldsymbol{u}}^{n+1}\right)$$
$$+ \frac{\sigma}{\epsilon_c}\mu^n\boldsymbol{\nabla}c^n - \frac{(1-\phi^{n+1})}{\epsilon^2}\left(\tilde{\boldsymbol{u}}^{n+1} - \boldsymbol{u}_g^{n+1}\right) + \phi^{n+1}\rho^{n+1}g\boldsymbol{z}, \tag{3.48}$$
$$dt\boldsymbol{\nabla}\cdot\left(\frac{\phi^{n+1}}{\rho^{n+1}}\boldsymbol{\nabla}p^{n+1}\right) = \boldsymbol{\nabla}\cdot\left(\phi^{n+1}\tilde{\boldsymbol{u}}^{n+1}\right) - \boldsymbol{u}_g^{n+1}\cdot\boldsymbol{\nabla}\phi^{n+1} + \alpha\boldsymbol{\nabla}\cdot\left(\phi^{n+1}M(c^{n+1})\boldsymbol{\nabla}\mu^{n+1}\right)$$
$$+ \alpha^2\boldsymbol{\nabla}\cdot\left(\phi^{n+1}M(c^{n+1})\boldsymbol{\nabla}p^{n+1}\right) - dt\boldsymbol{\nabla}\cdot\frac{(1-\phi^{n+1})}{\epsilon^2\rho^{n+1}}\left(\boldsymbol{u}^{n+1} - \tilde{\boldsymbol{u}}^{n+1}\right), \tag{3.49}$$
$$\boldsymbol{u}^{n+1} = \tilde{\boldsymbol{u}}^{n+1} - \frac{\phi^{n+1}\boldsymbol{\nabla}p^{n+1}}{\frac{\phi^{n+1}\rho^{n+1}}{dt} + \frac{(1-\phi^{n+1})}{\epsilon^2}}, \tag{3.50}$$
$$\frac{\phi^{n+1}c^{n+1} - \phi^n c^n}{dt} + \boldsymbol{\nabla}\cdot\left(\phi^n\boldsymbol{u}^n c^n\right) = \boldsymbol{\nabla}\cdot\left(\phi^{n+1}M(c^{n+1})\boldsymbol{\nabla}\mu^{n+1}\right)$$
$$+ \alpha\boldsymbol{\nabla}\cdot\left(\phi^{n+1}M(c^{n+1})\boldsymbol{\nabla}p^{n+1}\right), \tag{3.51}$$
$$\phi^{n+1}\mu^{n+1} = \phi^{n+1}\epsilon_c F'(c^{n+1}) - \epsilon_c^2\boldsymbol{\nabla}\cdot\left(\phi^{n+1}\boldsymbol{\nabla}c^{n+1}\right) - \frac{\epsilon_c|\nabla\phi^{n+1}|}{\sqrt{2}}\cos(\theta)\left(1-c^{n+1}\right)c^{n+1}, \tag{3.52}$$

with the following boundary conditions:

$$\tilde{\boldsymbol{u}}^{n+1}|_{\partial\Omega} = \boldsymbol{u}^{n+1}|_{\partial\Omega} = 0, \quad \boldsymbol{n}\cdot\boldsymbol{\nabla}p^{n+1}|_{\partial\Omega} = \boldsymbol{n}\cdot\boldsymbol{\nabla}c^{n+1}|_{\partial\Omega} = \boldsymbol{n}\cdot\boldsymbol{\nabla}\mu^{n+1}|_{\partial\Omega} = 0. \tag{3.53}$$

Here $\tilde{\boldsymbol{u}}$ is a temporary velocity that splits the original momentum equation Eq. (3.9). We first solve Eqs. (3.51) and (3.52) to get c^{n+1} and μ^{n+1} , we then obtain $\tilde{\boldsymbol{u}}^{n+1}$ and p^{n+1} from Eqs. (3.48) and (3.49). Finally the velocity $\boldsymbol{u}^{n+1}$ is updated in Eq. (3.50).

At the fully discrete level, our method is solved with the finite difference method on a staggered grid and implemented on an efficient, practical nonlinear multigrid solver. In particular, this is comprised of a standard FAS method for the Cahn-Hilliard equations Eqs. (3.51) and (3.52), and a method based on the Vanka-type smoothing strategy for the Navier-Stokes equations Eqs. (3.48)-(3.50) [38].

3.5 Numerical results

3.5.1 Cavity flow

We consider a two-phase fluid flow in a driven cavity [13]. The numerical results from the q-NSCH system (Eqs. (3.1)-(3.4)) on the physical domain $D = [0,1]^2$ are compared to those from the q-NSCH-DD system (Eqs. (3.9)-(3.12)) on an extended domain $\Omega = [-0.25, 1.25]^2$. The boundary conditions on ∂D are imposed as

$$\boldsymbol{u} = \boldsymbol{u}_g, \tag{3.54}$$

$$\boldsymbol{n}\cdot\boldsymbol{\nabla}(\mu + \alpha p) = 0, \tag{3.55}$$

$$\boldsymbol{n}\cdot\boldsymbol{\nabla}c = 0, \tag{3.56}$$

where $\boldsymbol{u}_g = (g_u, g_v) = (g_u, 0)$, and

$$g_u = \begin{cases} \max\left(0, 1 - 4 \times (x - 0.5)^2\right) & \text{if } y = 1, \\ 0 & \text{if } y < 1. \end{cases} \tag{3.57}$$

The function ϕ is given by

$$\begin{aligned} \phi =& 0.5 \left(1 + \tanh\left(\frac{3x}{\epsilon}\right)\right) \times 0.5 \left(1 + \tanh\left(\frac{3(1-x)}{\epsilon}\right)\right) \\ & \times 0.5 \left(1 + \tanh\left(\frac{3y}{\epsilon}\right)\right) \times 0.5 \left(1 + \tanh\left(\frac{3(1-y)}{\epsilon}\right)\right) \end{aligned} \tag{3.58}$$

to approximate the characteristic function of D, and g_u is extended to Ω as follows,

$$g_u(x, y) = \begin{cases} \max\left(0, 1 - 4 \times (x - 0.5)^2\right) & \text{if } y \leq 1 - \epsilon, \\ 0 & \text{if } y > 1 - \epsilon. \end{cases} \tag{3.59}$$

For both systems, the initial c is

$$c = \frac{1}{2}\left(1 - \tanh\left(\frac{0.5 - y}{2\sqrt{2}\epsilon_c}\right)\right), \tag{3.60}$$

such that $c = 0$ for the fluid at bottom and $c = 1$ for the top fluid. In addition, we set

$$\rho_1 = \rho_2 = 1, \quad \nu_1 = \nu_2 = 0.002, \quad g = 0, \quad \sigma = 0, \quad \theta = 90^\circ, \quad \text{and} \quad \epsilon_c = 0.05.$$

We present the evolution of the phase field variable c obtained from the q-NSCH-DD system in Fig. 3.1 and compare c at $t = 15$ with the one from the q-NSCH system at the same time in Fig. 3.2.

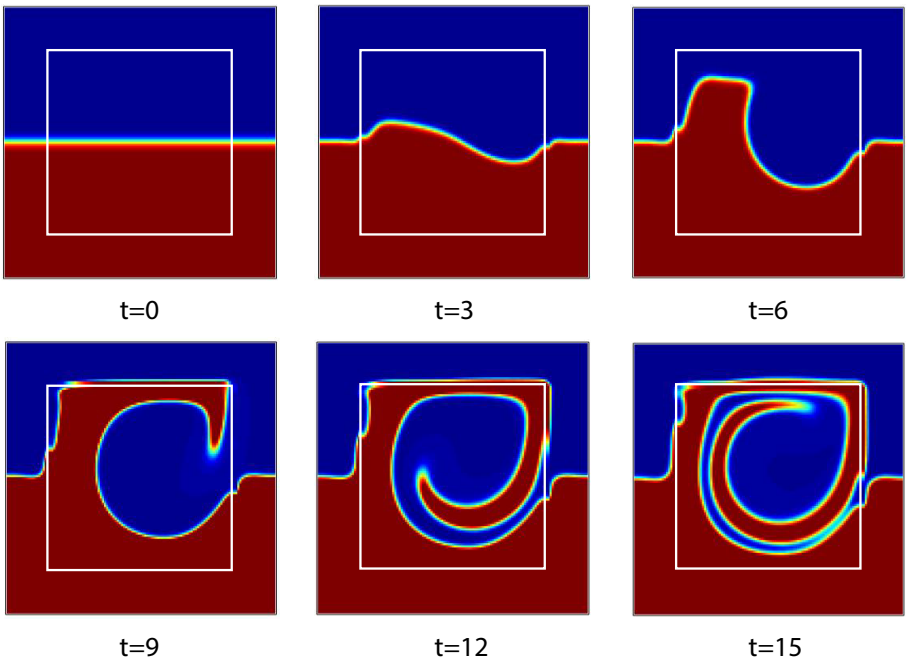

Figure 3.1: Evolution of the phase field variable c in a cavity flow. The results are obtained using the q-NSCH-DD system with the grid size $h = 1.5/256$, $dt = 2.5 \times 10^{-3}$ and $\epsilon = 0.025$ in Ω. The white box represents the physical domain D.

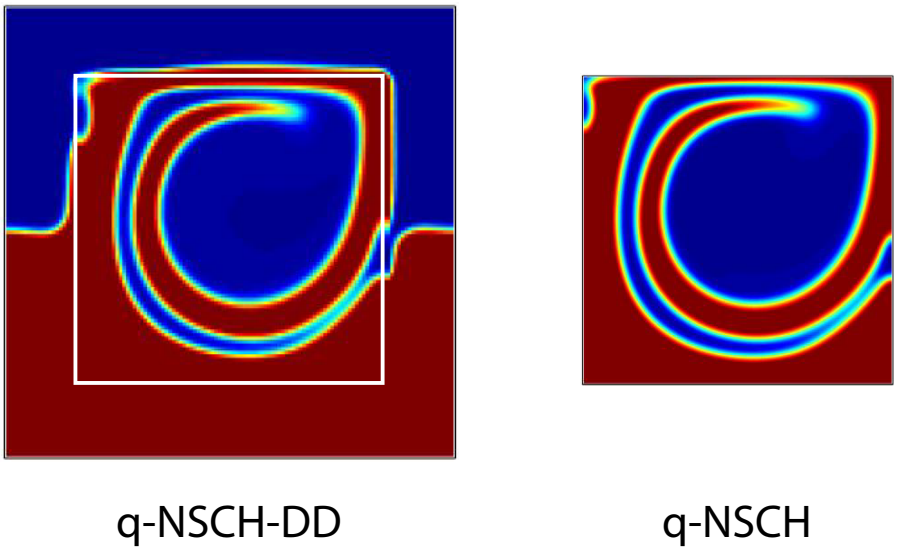

Figure 3.2: Comparisons between the phase field variable c obtained from the q-NSCH-DD system and the one from the q-NSCH system at $t = 15$. The white box represents the physical domain D.

Moreover, we use the results, including the velocities u, v, and phase variable c, from q-NSCH with the grid size $h = 1/1024$ and the time step $dt = 3.90625 \times 10^{-5}$ as the exact solutions. For the q-NSCH-DD system, we start with $h = 1.5/64$, $dt = 10^{-2}$ and $\epsilon = 0.1$, and refine them together. For each ϵ, we restrict the solutions from q-NSCH-DD to D and compute the errors in the L^2 and Ł$^\infty$ norms. The errors of the velocities u, v, and phase variable c at $t = 0.1$ are presented in Tables 3.1 and 3.2. We observe that our diffuse domain approximation converges to the q-NSCH model with $\mathcal{O}(\epsilon)$.

ϵ	u	$\boldsymbol{k}$	v	$\boldsymbol{k}$	c	$\boldsymbol{k}$
1.00E-01	5.17E-02		2.98E-02		1.09E-02	
5.00E-02	2.40E-02	1.11	1.73E-02	0.78	4.25E-03	1.36
2.50E-02	1.12E-02	1.10	8.90E-03	0.96	1.75E-03	1.28
1.25E-02	5.46E-03	1.04	4.32E-03	1.04	7.50E-04	1.22
6.25E-03	2.72E-03	1.01	2.17E-03	0.99	3.21E-04	1.22

Table 3.1: The L^2 errors of the velocities u, v and phase field variable c in a cavity flow in Sec. 3.5.1, see text for details..

ϵ	u	$\boldsymbol{k}$	v	$\boldsymbol{k}$	c	$\boldsymbol{k}$
1.00E-01	2.05E-01		9.80E-02		3.65E-02	
5.00E-02	1.22E-01	0.75	4.52E-02	1.12	1.47E-02	1.31
2.50E-02	6.64E-02	0.88	2.58E-02	0.81	6.13E-03	1.26
1.25E-02	3.44E-02	0.95	1.37E-02	0.91	2.66E-03	1.20
6.25E-03	1.74E-02	0.98	6.92E-03	0.99	1.15E-03	1.21

Table 3.2: The L^∞ errors of the velocities u, v and phase field variable c in a cavity flow in Sec. 3.5.1, see text for details..

3.5.2 Droplet on cylinder

We consider a circular droplet of diameter d wetting and dewetting on a solid cylinder. Initially, the droplet is placed on the cylinder of the same diameter d with contact angle $\theta_0 = 90^o$. With θ being the static contact angle, the contact line of the droplet recedes if $\theta < \theta_0$ or spreads if $\theta > \theta_0$, and eventually reaches the equilibrium with the interface intersecting the solid cylinder at an angle of θ. In the absence of gravity, the equilibrium state of the droplet can be obtained analytically by carving the cylinder out the a circle [55, 63] (see Fig. 3.3). The distance between the centers of the circle and the cylinder, d_c, and the diameter of the circle, d_l, can be computed by solving

$$\pi d^2/4 = (\alpha + \theta)(d_l/2) - \alpha(d/2)^2 + (d_l d/4)\sin\theta, \tag{3.61}$$

$$d_l = d\cos\theta + \sqrt{d^2\cos^2\theta - d^2 + 4d_c^2}, \tag{3.62}$$

where

$$\alpha = \arccos\left(\frac{d^2 + 4d_c^2 - d_l^2}{4dd_c}\right). \tag{3.63}$$

Here we replace the term $\phi\boldsymbol{\nabla}(\nu\boldsymbol{\nabla}\cdot\boldsymbol{u})$ in Eq. (3.9) with $\boldsymbol{\nabla}(\phi\nu\boldsymbol{\nabla}\cdot\boldsymbol{u})$ and test another diffuse-domain approximation to the q-NSCH system, namely q-NCSH-DD-M. We solve q-NCSH-DD-M in a larger domain $\Omega = [0, 2d] \times [0, 2d]$. The initial ϕ and c are given by

$$\phi = \frac{1}{2}\left(1 + \tanh\left(\frac{3(r_\phi - 0.5d)}{\epsilon}\right)\right), \quad \text{and} \quad c = \frac{1}{2}\left(1 + \tanh\left(\frac{r_c - 0.5d}{2\sqrt{2}\epsilon_c}\right)\right) \times \phi, \tag{3.64}$$

where $r_\phi = \sqrt{(x - 0.5d)^2 + (y - 0.6d)^2}$ and $r_c = \sqrt{(x - 0.5d)^2 + (y - 0.6d - 0.5\sqrt{2}d)^2}$, such that $c = 1$ for the droplet and $c = 0$ for the medium fluid. All the other parameters are set

as the following:

$$\rho_1 = 1000,\ \rho_2 = 1,\ \mu_1 = \mu_2 = 0.1,\ \sigma = 1,\ g = 0,\ \epsilon_c = \epsilon.$$

In Fig. 3.3, we compare numerical solutions ϕc at equilibrium from the q-NSCH-DD-M system with the analytical solutions, obtained from Eqs. (3.61)-(3.63), for various θ with the number of grid points $n = 2048$ in each direction. The L^2 errors, E_c, are also presented in Tab. 3.3 by refining n and $\epsilon = \epsilon_c$ together. We find that our q-NSCH-DD-M system provides a first order approximation to the exact solution.

		30^o		90^o		120^o	
ϵ	n	E_c	rate	E_c	rate	E_c	rate
0.02	128	4.32×10^{-2}	—	4.95×10^{-2}	—	5.51×10^{-2}	—
0.01	256	2.85×10^{-2}	0.60	3.22×10^{-2}	0.62	3.61×10^{-2}	0.61
0.005	512	1.79×10^{-2}	0.67	1.98×10^{-2}	0.70	2.33×10^{-2}	0.63
0.0025	1024	1.05×10^{-2}	0.77	1.18×10^{-2}	0.75	1.35×10^{-2}	0.79
0.00125	2048	5.29×10^{-3}	0.99	6.00×10^{-3}	0.98	7.04×10^{-3}	0.94

Table 3.3: The L^2 errors of the phase field variable restricted on D, ϕc, at equilibrium with different static contact angles, 30^o, 90^o and 120^o.

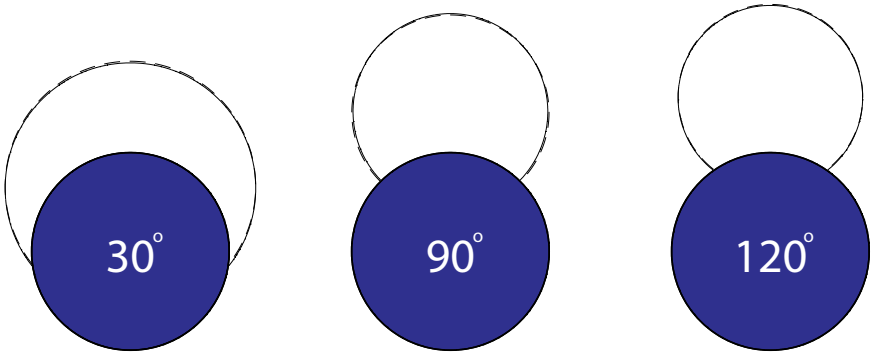

Figure 3.3: Comparisons between the numerical results at equilibrium (solid lines) and the analytic solutions (dashed lines) with different static contact angles, where the angles are indicated inside the blue cylinders.

3.5.3 Penetration of a liquid droplet into porous media

We consider a two-dimensional droplet impacting on to a porous substrate consisting of three cylinders (C_i, i=1,2,3) with different wettability, as shown in Fig. 3.4. The extended domain $\Omega = [0,1] \times [0,1]$ and is discretized on a uniform mesh of $[1024 \times 1024]$. The original physical domain $D = \Omega/(\cup C_i)$. There are three cylinders in the domain with radii $r_1 = 0.1$, $r_2 = 0.12$, $r_3 = 0.15$, and centers $(0.3, 0.6)$, $(0.4, 0.25)$, $(0.7, 0.5)$, respectively. Initially, a heavy liquid drop with radius $r_d = 0.15$ is placed above the cylinders with the center $(0.5, 0.8)$. Note that the initial ϕ and c can be given by a slight modification of Eq. (3.64). Again, we let $c = 1$ stands for the heavy fluid droplet, and $c = 0$ stands for the light fluid medium. All other parameters are set as follows:

$$\rho_1 = 1000,\ \rho_2 = 1,\ \mu_1 = 10,\ \mu_2 = 0.1,\ g = 1,\ \epsilon_c = 0.001\ \epsilon = 0.002. \tag{3.65}$$

The dynamics of droplet impact is shown in Fig. 3.4 in terms of snapshots at different times. Initially, the droplet starts moving downwards due to the gravitational forces. Dramatic deformations are observed when the droplet comes into contact with the left and right

cylinders, respectively. After impacting on the cylinder at the bottom, the droplet split into several parts. In the end, it is interesting to see that there is no liquid on the cylinders with wettability of $\theta = 90^o$ and $\theta = 120^o$. All the liquid rests either on the cylinder with $\theta = 60^o$ or on the walls.

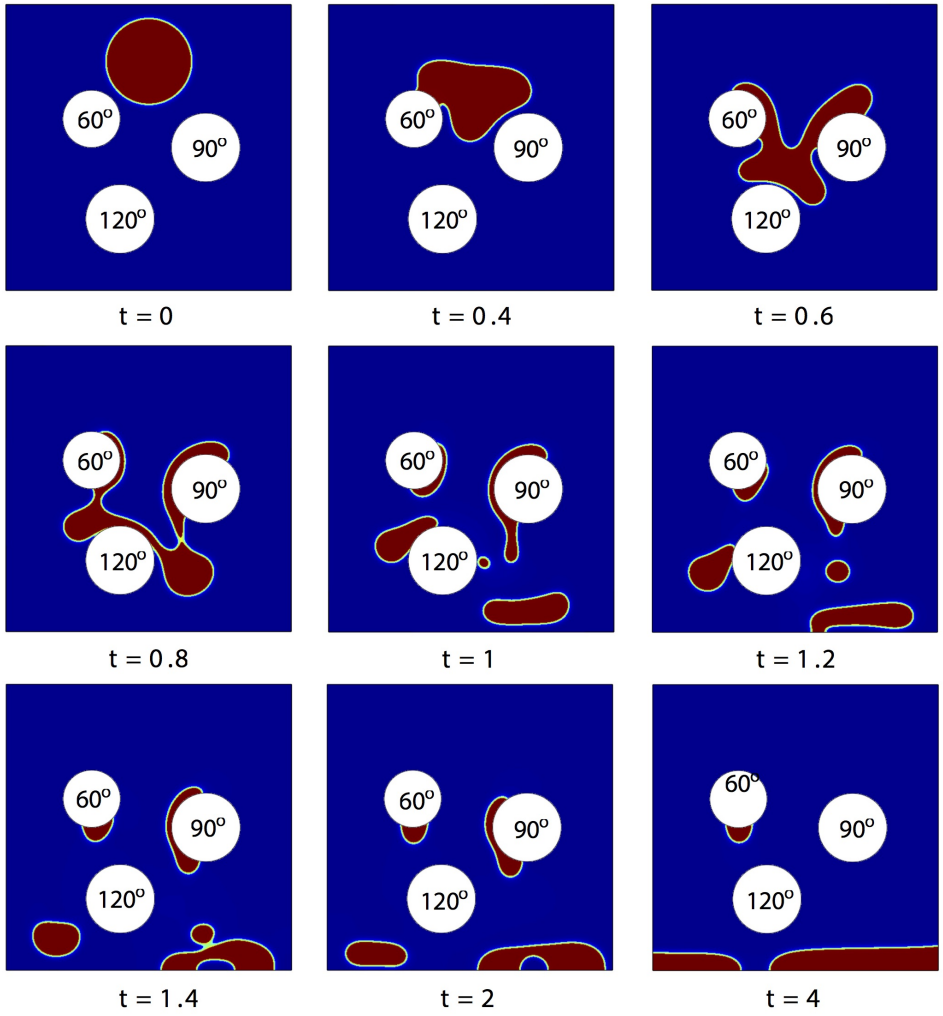

Figure 3.4: Dynamics of a two-dimensional droplet on three cylinders with different wettability. The static contact angles θ are indicated inside the corresponding cylinder. The red stands for the heavy fluid and the blue stands for the light fluid medium.

Chapter 4

Conclusion and Discussion

In the first part of this thesis, we have analyzed several diffuse domain methods (DDMs) originally developed in [53] for both the Poisson equation and the diffusion equation with Dirchlet boundary conditions on stationary and moving domains. The level-set method was used to implicitly capture the domain movement and to construct the smoothed characteristic function needed by the methods. Our analysis reveals why the different formulations yield varying degrees of accuracy. Guided by our analysis, we presented new modifications of the DDMs (mDDMs) that provide higher-order accuracy. Using a matched asymptotic analysis, two of these methods, mDDM1 and mDDM3, were shown to be 2nd order accurate in L^2, e.g., $\mathcal{O}(\epsilon^2)$ where ϵ is the diffuse interface smoothing parameter. The analysis shows that the errors in the L^∞ norm scale as $\mathcal{O}(\epsilon^{1.5})$. Using numerical simulations in both 1D and 2D for selected test cases, these theoretical predictions were confirmed when the grid size $h \sim \epsilon^{1.5}$ is used to resolve the boundary layer (e.g., K_3 in Sec. 2.1.3.1). In addition, numerical simulations revealed that in the L^2 norm, mDDM1 and mDDM3 and their time-dependent versions (mDDMt1, mDDMt3) are $\mathcal{O}(\epsilon^2)$ even when $h \propto \epsilon$, which is much cheaper computationally and hence more cost-effective to use for 2D and 3D problems. In this case, however, the L^∞ errors were found to be more variable over the range of parameters tested.

In L^∞, simulations with $h = \epsilon/c$ show that when $c \sim 1$, the schemes are roughly $O(\epsilon^2)$. This occurs because even though the the boundary layer (K_3) is not resolved the numerical solutions are actually closer to the exact solution near the boundary of the complex domain. When $c >> 1$, the boundary layer is better resolved, the numerical solutions are smoother and deviate more near the boundary from the exact solution, which ultimately results in errors that scale as $\mathcal{O}(\epsilon^{1.5})$ as predicted by theory.

In the second part, starting with a thermodynamically consistent diffuse interface model, the q-NSCH system, we proposed a diffuse domain approximation to the model, namely the q-NSCH-DD system, to simulate two-phase flows with variable density and viscosity in complex geometries. We found that the q-NSCH-DD system converges to q-NSCH as the thickness of the diffuse domain interface shrink to zero ($\epsilon \to 0$). The q-NSCH-DD system is solved on a larger, regular domain using an existing finite difference multigrid solver without any modification on a staggered grid and the numerical results confirmed our analysis. We also observed that the q-NSCH-DD system not only allows the contact line to move on the curved boundaries, but also makes the fluid-fluid interface to intersect the solid object at an angle which is consistent with the prescribed contact angle.

In the future, we plan to apply the mDDMs developed in Chapter 2 on the fluid problems in Chapter 3 to achieve higher order accuracy in ϵ. We also would like to give a theoretical proof for the higher-order mDDMs.

Bibliography

[1] H. Abels, K. Lam, and B. Stinner. Analysis of the diffuse domain approach for a bulk-surface coupled pde system. *SIAM J. Math. Anal.*, 47(5):3687–3725, 2015.

[2] S. Aland, S. Egerer, J. Lowengrub, and A. Voigt. Diffuse interface models of locally inextensible vesicles in a viscous fluid. *J. Comput. Phys.*, 277:32–47, 2014.

[3] S. Aland, C. Landsberg, R. Mueller, F. Stenger, M. Bobeth, A. Langheinrich, and A. Voigt. Adaptive diffuse domain approach for calculating mechanically induced deformation of trabecular bone. *Comp. Meth. Biomech. Biomed. Eng.*, 17(1):31–38, 2011.

[4] S. Aland, J. Lowengrub, and A. Voigt. Two-phase flow in complex geometries: A diffuse domain approach. *CMES-COMPUTER MODELING IN ENGINEERING & SCIENCES*, 57(1):77–107, FEB 2010.

[5] S. Aland, J. Lowengrub, and A. Voigt. A continuum model of colloid-stabilized interfaces. *Phys. Fluids*, 23(6):062103, 2011.

[6] S. Aland, J. Lowengrub, and A. Voigt. Particles at fluid-fluid interfaces: A new navier-stokes-cahn-hilliard surface-phase-field-crystal model. *Phys. Rev. E*, 86(4):046321, 2012.

[7] S. Amat, Z. Li, and J. Ruiz. On an New Algorithm for Function Approximation with Full Accuracy in the Presence of Discontinuities Based on the Immersed Interface Method. *JOURNAL OF SCIENTIFIC COMPUTING*, 75(3):1500–1534, JUN 2018.

[8] T. Askham and A. J. Cerfon. An adaptive fast multipole accelerated Poisson solver for complex geometries. *JOURNAL OF COMPUTATIONAL PHYSICS*, 344:1–22, SEP 1 2017.

[9] A. J. Barlow, P.-H. Maire, W. J. Rider, R. N. Rieben, and M. J. Shashkov. Arbitrary Lagrangian-Eulerian methods for modeling high-speed compressible multimaterial flows. *JOURNAL OF COMPUTATIONAL PHYSICS*, 322:603–665, OCT 1 2016.

[10] T. Belytschko, R. Gracie, and G. Ventura. A review of extended/generalized finite element methods for material modeling. *MODELLING AND SIMULATION IN MATERIALS SCIENCE AND ENGINEERING*, 17(4), JUN 2009.

[11] C. M. Bender and S. A. Orszag. *Advanced mathematical methods for scientists and engineers I: Asymptotic methods and perturbation theory*. Springer Science & Business Media, 2013.

[12] W. Bo and M. Shashkov. Adaptive reconnection-based arbitrary Lagrangian Eulerian method. *JOURNAL OF COMPUTATIONAL PHYSICS*, 299:902–939, OCT 15 2015.

[13] F. Boyer. A theoretical and numerical model for the study of incompressible mixture flows. *Computers & Fluids*, 31(1):41 – 68, 2002.

[14] A. Bueno-Orovio and V. Perez-Garcia. Spectral smoothed boundary methods: The role of external boundary conditions. *Numer. Meth. Partial Diff. Eqns.*, 22:435–448, 2005.

[15] A. Bueno-Orovio, V. Perez-Garcia, and F. Fenton. Spectral methods for partial differential equations in irregular domains: The spectral smoothed boundary method. *SIAM J. Sci. Comput.*, 28:886–900, 2006.

[16] M. Burger, O. Elvetun, and M. Schlottbom. Analysis of the diffuse domain method for second order elliptic boundary value problems. *Found. Comput. Math.*, 17:627–674, 2017.

[17] A. Calderer, S. Kang, and F. Sotiropoulos. Level set immersed boundary method for coupled simulation of air/water interaction with complex floating structures. *JOURNAL OF COMPUTATIONAL PHYSICS*, 277:201–227, NOV 15 2014.

[18] B. Camley, Y. Zhao, B. Li, H. Levine, and W.-J. Rappel. Periodic migration in a physical model of cells on micropatterns. *Phys. Rev. Lett.*, 111:158102, 2013.

[19] B. Camley, Y. Zhao, B. Li, H. Levine, and W.-J. Rappel. Crawling and turning in a minimal reaction-diffusion cell motility model: Coupling cell shape and biochemistry. *Phys. Rev. E*, 95:012401, 2017.

[20] J. Carlos Martinez, L. V. Vanegas Useche, and M. A. Wahab. Numerical prediction of fretting fatigue crack trajectory in a railway axle using XFEM. *INTERNATIONAL JOURNAL OF FATIGUE*, 100(1):32–49, JUL 2017.

[21] A. Chadwick, J. Steward, R. Du, and K. Thornton. Numerical modeling of localized corrosion using phase-field and smoothed boundary methods. *J. Electrochemical Soc.*, 165(10):C633–C646, 2018.

[22] L. Chen, H. Wei, and M. Wen. An interface-fitted mesh generator and virtual element methods for elliptic interface problems. *JOURNAL OF COMPUTATIONAL PHYSICS*, 334:327–348, APR 1 2017.

[23] Y. Chen and J. Lowengrub. Tumor growth in complex, evolving microenvironmental geometries: A diffuse domain approach. *J. Theor. Biol.*, 361:14–30, 2014.

[24] J. Favier, A. Revell, and A. Pinelli. A Lattice Boltzmann-Immersed Boundary method to simulate the fluid interaction with moving and slender flexible objects. *JOURNAL OF COMPUTATIONAL PHYSICS*, 261:145–161, MAR 15 2014.

[25] R. Fedkiw, T. Aslam, B. Merriman, and S. Osher. A non-oscillatory Eulerian approach to interfaces in multimaterial flows (the ghost fluid method). *JOURNAL OF COMPUTATIONAL PHYSICS*, 152(2):457–492, JUL 1 1999.

[26] M. Feischl, T. Fuehrer, N. Heuer, M. Karkulik, and D. Praetorius. Adaptive boundary element methods a posteriori error estimators, adaptivity, convergence, and implementation. *Arch. Comp. Meth. Eng.*, 22(3):309–389, 2015.

[27] F. Fenton, E. Cherry, A. Karma, and W.-J. Rappel. Modeling wave propagation in realistic heart geometries using the phase-field method. *Chaos*, 15:013502, 2005.

[28] S. Franz, H.-G. Roos, R. Gärtner, and A. Voigt. A note on the convergence analysis of a diffuse-domain approach. *COMPUTATIONAL METHODS IN APPLIED MATHEMATICS*, 12(2):153–167, 2012.

[29] T.-P. Fries and T. Belytschko. The extended/generalized finite element method: An overview of the method and its applications. *INTERNATIONAL JOURNAL FOR NUMERICAL METHODS IN ENGINEERING*, 84(3):253–304, OCT 15 2010.

[30] P. Galenko, D. Alexandrov, and E. Titova. The boundary integral theory for slow and rapid curved solid/liquid interfaces propagating into binary systems. *Phil. Trans. Roy. Soc. A*, 376(2113):20170218, 2018.

[31] S. Gallier, E. Lemaire, L. Lobry, and F. Peters. A fictitious domain approach for the simulation of dense suspensions. *JOURNAL OF COMPUTATIONAL PHYSICS*, 256:367–387, JAN 1 2014.

[32] Z. Ge, J.-C. Loiseau, O. Tammisola, and L. Brandt. An efficient mass-preserving interface-correction level set/ghost fluid method for droplet suspensions under depletion forces. *JOURNAL OF COMPUTATIONAL PHYSICS*, 353:435–459, JAN 15 2018.

[33] F. Gibou, R. Fedkiw, and S. Osher. A review of level-set methods and some recent applications. *J. Comput. Phys.*, 353:82–109, 2018.

[34] R. GLOWINSKI, T. PAN, and J. PERIAUX. A FICTITIOUS DOMAIN METHOD FOR DIRICHLET PROBLEM AND APPLICATIONS. *COMPUTER METHODS IN APPLIED MECHANICS AND ENGINEERING*, 111(3-4):283–303, JAN 1994.

[35] N. Gokhale, N. Nikiforakis, and R. Klein. A dimensionally split Cartesian cut cell method for hyperbolic conservation laws. *JOURNAL OF COMPUTATIONAL PHYSICS*, 364:186–208, JUL 1 2018.

[36] S. Gottlieb and C. Shu. Total variation diminishing Runge-Kutta schemes. *MATHEMATICS OF COMPUTATION*, 67(221):73–85, JAN 1998.

[37] A. Guittet, M. Lepilliez, S. Tanguy, and F. Gibou. Solving elliptic problems with discontinuities on irregular domains - the Voronoi Interface Method. *JOURNAL OF COMPUTATIONAL PHYSICS*, 298:747–765, OCT 1 2015.

[38] Z. Guo, P. Lin, J. Lowengrub, and S. M. Wise. Mass conservative and energy stable finite difference methods for the quasi-incompressible Navier-Stokes-Cahn-Hilliard system: Primitive variable and projection-type schemes. *COMPUTER METHODS IN APPLIED MECHANICS AND ENGINEERING*, 326:144–174, NOV 1 2017.

[39] Z. Guo, F. Yu, P. Lin, S. Wise, and J. Lowengrub. A diffuse domain approach for two phase flows with large density ratio in complex geometries. *in preparation*, 2018.

[40] C. Hirt, A. Amsden, and J. Cook. An arbitrary Lagrangian-Eulerian computing method for all flow speeds (Reprinted from the Journal of Computational Physics, vol 14, pg 227-253, 1974). *JOURNAL OF COMPUTATIONAL PHYSICS*, 135(2):203–216, AUG 1997.

[41] J. D. Hoffman and S. Frankel. *Numerical methods for engineers and scientists*. CRC press, 2001.

[42] L. Hong, L. Liang, S. Bhattacharyya, W. Xing, and L.-Q. Chen. Anisotropic li intercalation in a lixfepo4 nano-particle: a spectral smoothed boundary phase-field model. *Phys, Chem. Chem. Phys.*, 18:9537–9543, 2016.

[43] R. Hu and Z. Li. Error analysis of the immersed interface method for Stokes equations with an interface. *APPLIED MATHEMATICS LETTERS*, 83:207–211, SEP 2018.

[44] D. Ingram, D. Causon, and C. Mingham. Developments in Cartesian cut cell methods. *MATHEMATICS AND COMPUTERS IN SIMULATION*, 61(3-6):561–572, JAN 30 2003. 2nd IMACS Conference on Mathematical Modelling and Computational Methods in Mechanics, Physics, Biomechanics and Geodynamics, PLZEN, CZECH REPUBLIC, JUN 19-25, 2001.

[45] M. Irfan and M. Muradoglu. A front tracking method for direct numerical simulation of evaporation process in a multiphase system. *JOURNAL OF COMPUTATIONAL PHYSICS*, 337:132–153, MAY 15 2017.

[46] G. Jiang and C. Shu. Efficient implementation of weighted ENO schemes. *JOURNAL OF COMPUTATIONAL PHYSICS*, 126(1):202–228, JUN 1996.

[47] Y. Jiang, P. Lin, Z. Guo, and S. Dong. Numerical Simulation for Moving Contact Line with Continuous Finite Element Schemes. *Communications in Computational Physics*, 18(01):180–202, 2015.

[48] C. Klingenberg, G. Schnucke, and Y. Xia. An Arbitrary Lagrangian-Eulerian Local Discontinuous Galerkin Method for Hamilton-Jacobi Equations. *JOURNAL OF SCIENTIFIC COMPUTING*, 73(2-3, SI):906–942, DEC 2017.

[49] J. Kockelkoren, H. Levine, and W.-J. Rappel. Computational approach for modeling intra- and computational approach for modeling intra- and extracellular dynamics. *Phys. Rev. E*, 68:037702, 2003.

[50] B. Lalanne, L. R. Villegas, S. Tanguy, and F. Risso. On the computation of viscous terms for incompressible two-phase flows with Level Set/Ghost Fluid Method. *JOURNAL OF COMPUTATIONAL PHYSICS*, 301:289–307, NOV 15 2015.

[51] K. Y. Lervåg and J. Lowengrub. Analysis of the diffuse-domain method for solving PDEs in complex geometries. *COMMUNICATIONS IN MATHEMATICAL SCIENCES*, 13(6):1473–1500, 2015.

[52] R. LEVEQUE and Z. LI. The immersed interface method for elliptic equations with discontinuous coefficients and singular sources. *SIAM JOURNAL ON NUMERICAL ANALYSIS*, 31(4):1019–1044, AUG 1994.

[53] X. Li, J. Lowengrub, A. Raetz, and A. Voigt. Solving PDEs in complex geometries: a diffuse domain approach. *COMMUNICATIONS IN MATHEMATICAL SCIENCES*, 7(1):81–107, MAR 2009.

[54] Z. Li, M.-C. Lai, X. Peng, and Z. Zhang. A least squares augmented immersed interface method for solving Navier-Stokes and Darcy coupling equations. *COMPUTERS & FLUIDS*, 167:384–399, MAY 15 2018.

[55] H.-R. Liu and H. Ding. A diffuse-interface immersed-boundary method for two-dimensional simulation of flows with moving contact lines on curved substrates. *Journal of Computational Physics*, 294:484 – 502, 2015.

[56] J. Lowengrub, J. Allard, and S. Aland. Numerical simulation of endocytosis: Viscous flow driven by membranes with non-uniformly distributed curvature-inducing molecules. *J. Comput. Phys.*, 309:112–128, 2016.

[57] A. Massing, M. G. Larson, A. Logg, and M. E. Rognes. A Stabilized Nitsche Fictitious Domain Method for the Stokes Problem. *JOURNAL OF SCIENTIFIC COMPUTING*, 61(3):604–628, DEC 2014.

[58] C. Min. On reinitializing level set functions. *JOURNAL OF COMPUTATIONAL PHYSICS*, 229(8):2764–2772, APR 20 2010.

[59] R. Mittal and G. Iaccarino. Immersed boundary methods. *ANNUAL REVIEW OF FLUID MECHANICS*, 37:239–261, 2005.

[60] B. Muralidharan and S. Menon. Simulation of moving boundaries interacting with compressible reacting flows using a second-order adaptive Cartesian cut-cell method. *JOURNAL OF COMPUTATIONAL PHYSICS*, 357:230–262, MAR 15 2018.

[61] F. Nikfarjam, Y. Cheny, and O. Botella. The LS-STAG immersed boundary/cut-cell method for non-Newtonian flows in 3D extruded geometries. *COMPUTER PHYSICS COMMUNICATIONS*, 226:67–80, MAY 2018.

[62] N. Noormohammadi and B. Boroomand. A fictitious domain method using equilibrated basis functions for harmonic and bi-harmonic problems in physics. *JOURNAL OF COMPUTATIONAL PHYSICS*, 272:189–217, SEP 1 2014.

[63] A. O'Brien and M. Bussmann. A volume-of-fluid ghost-cell immersed boundary method for multiphase flows with contact line dynamics. *Computers & Fluids*, 165:43 – 53, 2018.

[64] S. Osher and J. A. Sethian. Fronts propagating with curvature-dependent speed-algorithms based on hamilton-jacobi formulations. *J. Comput. Phys.*, 79(1):12–49, 1988.

[65] D. Peng, B. Merriman, S. Osher, H. Zhao, and M. Kang. A PDE-based fast local level set method. *JOURNAL OF COMPUTATIONAL PHYSICS*, 155(2):410–438, NOV 1 1999.

[66] S. Poulsen and P. Voorhees. Smoothed boundary method for diffusion-related partial differential equations in complex geometries. *Int. J. Comput. Meth.*, 15(3):1850014, 2018.

[67] A. Raetz. A new diffuse-interface model for step flow in epitaxial growth. *IMA J. Appl. Math.*, 80(3):697–711, 2015.

[68] A. Raetz. Diffuse-interface approximations of osmosis free boundary problems diffuse-interface approximations of osmosis free boundary problems. *SIAM J. Appl. Math.*, 76(3):910–929, 2016.

[69] A. Raetz and M. Roeger. Symmetry breaking in a bulk-surface reaction-diffusion model for signaling networks. *Nonlinearity*, 27:1805–1827, 2014.

[70] A. Raetz and A. Voigt. Pde's on surfaces — a diffuse interface approach. *Comm. Math. Sci.*, 4(3):575–590, 2006.

[71] G. Russo and P. Smereka. A remark on computing distance functions. *JOURNAL OF COMPUTATIONAL PHYSICS*, 163(1):51–67, SEP 1 2000.

[72] R. I. Saye and J. A. Sethian. Analysis and applications of the Voronoi Implicit Interface Method. *JOURNAL OF COMPUTATIONAL PHYSICS*, 231(18):6051–6085, JUL 15 2012.

[73] M. Schlottbom. Error analysis of a diffuse interface method for elliptic problems with dirichlet boundary conditions. *Appl. Num. Math.*, 109:109–122, 2016.

[74] H. Shahin and S. Mortazavi. Three-dimensional simulation of microdroplet formation in a co-flowing immiscible fluid system using front tracking method. *JOURNAL OF MOLECULAR LIQUIDS*, 243:737–749, OCT 2017.

[75] D. B. Stein, R. D. Guy, and B. Thomases. Immersed Boundary Smooth Extension (IBSE): A high-order method for solving incompressible flows in arbitrary smooth domains. *JOURNAL OF COMPUTATIONAL PHYSICS*, 335:155–178, APR 15 2017.

[76] K. E. Teigen, X. Li, J. Lowengrub, F. Wang, and A. Voigt. A diffuse-interface approach for modeling transport, diffusion and adsorption/desorption of material quantities on a deformable interface. *COMMUNICATIONS IN MATHEMATICAL SCIENCES*, 7(4):1009–1037, DEC 2009.

[77] K. E. Teigen, P. Song, J. Lowengrub, and A. Voigt. A diffuse-interface method for two-phase flows with soluble surfactants. *JOURNAL OF COMPUTATIONAL PHYSICS*, 230(2):375–393, JAN 20 2011.

[78] G. Tryggvason, B. Bunner, A. Esmaeeli, D. Juric, N. Al-Rawahi, W. Tauber, J. Han, S. Nas, and Y. Jan. A front-tracking method for the computations of multiphase flow. *JOURNAL OF COMPUTATIONAL PHYSICS*, 169(2):708–759, MAY 20 2001.

[79] L. R. Villegas, R. Alis, M. Lepilliez, and S. Tanguy. A Ghost Fluid/Level Set Method for boiling flows and liquid evaporation: Application to the Leidenfrost effect. *JOURNAL OF COMPUTATIONAL PHYSICS*, 316:789–813, JUL 1 2016.

[80] S. Wise, J. Kim, and J. Lowengrub. Solving the regularized, strongly anisotropic Cahn-Hilliard equation by an adaptive nonlinear multigrid method. *JOURNAL OF COMPUTATIONAL PHYSICS*, 226(1):414–446, SEP 10 2007.

[81] H.-C. Yu, H.-Y. Chen, and K. Thornton. Extended smoothed boundary method for solving partial differential equations with general boundary conditions on complex boundaries. *MODELLING AND SIMULATION IN MATERIALS SCIENCE AND ENGINEERING*, 20:075008, 2012.

[82] H.-C. Yu, M.-J. Choe, G. Amatucci, Y.-M. Chiang, and K. Thornton. Smoothed boundary method for simulating bulk and grain boundary transport in complex polycrystalline microstructures. *Comput. Mater. Sci.*, 121:14–22, 2016.

Appendix A

Additional numerical results of DDMs for 1D Poisson equations

We have tested the following three DDMs using $h = \epsilon/4$:

DDM1: $\nabla(\phi\nabla u) - \frac{1}{\epsilon^3}(1-\phi)(u-g) = \phi f$,

DDM2: $\phi\Delta u - \frac{1}{\epsilon^2}(1-\phi)(u-g) = \phi f$,

DDM3: $\nabla(\phi\nabla u) - \frac{1}{\epsilon^2}|\nabla\phi|(u-g) = \phi f$,

on the following seven cases,

Case1: $u = \frac{x^2}{2}$;

Case2: $u = (x^2 - 1.111)^2$;

Case3: $u = \frac{1}{x^2+1}$;

Case4: $u = \cos(x)$;

Case5: $u = (x^2+1)^2$;

Case6: $u = \log(x^2+1)$;

Case7: $u = \sqrt{x^2+1}$.

The original Poisson equation with Dirichlet boundary condition is again defined on $[-1.111, 1.111]$ and we solve the DDMs on a larger domain $[-2, 2]$. Tables A.1 - A.6 show the L^2 and L^∞ norms of errors for the three DDMs for the seven cases. In case 3-7, the convergence orders in both L^2 and L^∞ of DDM1-3 are similar to those in case 1. However in case 2, where the derivative of the exact solution is 0 at the boundary ($A = 0$), we observe 2nd order convergence in DDM2 and higher that 1st order convergence for DDM1 and DDM3. Our analysis in Sec. 2.1.2 indicates $\bar{u}_1^{(1)}(0) = \frac{A}{3}(-\ln 6 + \gamma)$ (Eq. (2.42)), $-\frac{A}{6}\ln\epsilon + \frac{A}{3}(-\ln 6 + \gamma)$ (Eq. (2.72)) and $-\frac{A}{6}\ln\epsilon + \frac{A}{3}(-\ln(\frac{1}{2}\sqrt{\frac{2}{3}}) + \gamma)$ (Eq. (2.74)) for DDM2, DDM1 and DDM3, respectively, which all vanish when $A = 0$. Hence, DDMs can achieve higher than 1st order accuracy when $A = 0$. In fact, the errors in both norms for DDM1 and DDM3 are dominated by $\mathcal{O}(\epsilon^2(\ln(\epsilon))^2)$. This term rises in the next order matching in K_2, that is $\lim_{z_2\to-\infty} \hat{u}_2^{(2)} = \bar{u}_2^{(2)}(0) + (z_2 + \ln\epsilon/6)^2 \frac{d^2}{dx^2}\bar{u}_1^{(0)}(0) + ...$ Thus $\bar{u}_2^{(2)}(0) \sim \mathcal{O}((\ln\epsilon)^2)$. In Fig. A.1(a), we plot $D(\epsilon) = \lim_{z_2\to-\infty}(u_\epsilon - u)/\epsilon^2$ versus $\ln(\epsilon)$ using the numerical solution of DDM1 in case 1 and find that it is a quadratic function of $\ln(\epsilon)$.

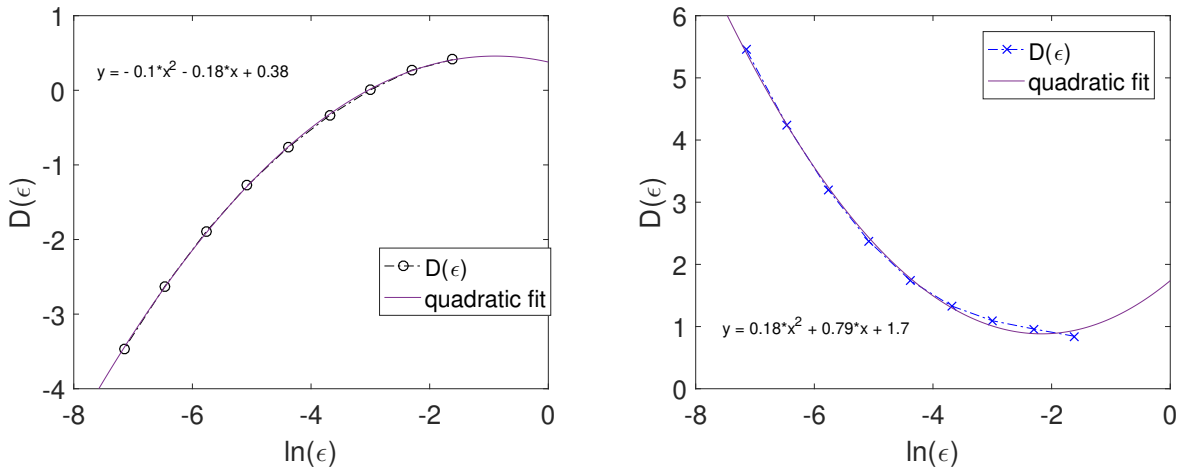

(a) (b)

Figure A.1: (a): $D(\epsilon)$ for DDM1 in case 1, (b): $D(\epsilon)$ for mDDM1 in case 1.

ϵ	**case 1**	**k**	**case 2**	**k**	**case 3**	**k**
2.00E-01	4.88E-01	0.00	1.55E-02	0.00	6.79E-02	0.00
1.00E-01	1.12E-01	2.12	2.75E-03	2.50	1.59E-02	2.10
5.00E-02	9.88E-03	3.51	9.39E-05	4.87	1.40E-03	3.51
2.50E-02	1.31E-02	-0.41	1.93E-04	-1.04	1.87E-03	-0.43
1.25E-02	1.41E-02	-0.11	1.15E-04	0.75	2.02E-03	-0.10
6.25E-03	1.04E-02	0.44	4.94E-05	1.22	1.49E-03	0.44
3.13E-03	6.80E-03	0.62	1.85E-05	1.41	9.70E-04	0.62
1.56E-03	4.16E-03	0.71	6.46E-06	1.52	5.94E-04	0.71

case 4	**k**	**case 5**	**k**	**case 6**	**k**	**case 7**	**k**
1.25E-01	0.00	4.88E-01	0.00	3.03E-01	0.00	7.32E-02	0.00
2.95E-02	2.08	1.13E-01	2.10	6.97E-02	2.12	1.72E-02	2.09
2.63E-03	3.49	1.01E-02	3.49	6.09E-03	3.52	1.52E-03	3.50
3.52E-03	-0.42	1.33E-02	-0.40	8.11E-03	-0.41	2.03E-03	-0.42
3.80E-03	-0.11	1.44E-02	-0.11	8.72E-03	-0.10	2.19E-03	-0.11
2.81E-03	0.43	1.07E-02	0.43	6.44E-03	0.44	1.62E-03	0.43
1.83E-03	0.62	6.95E-03	0.62	4.19E-03	0.62	1.06E-03	0.62
1.12E-03	0.71	4.25E-03	0.71	2.57E-03	0.71	6.46E-04	0.71

Table A.1: The L^2 errors for DDM1

ϵ	**case 1**	**k**	**case 2**	**k**	**case 3**	**k**
2.00E-01	2.12E-01	0.00	1.09E-02	0.00	5.36E-02	0.00
1.00E-01	5.26E-02	2.01	1.93E-03	2.49	1.28E-02	2.07
5.00E-02	7.96E-03	2.72	8.82E-05	4.45	1.93E-03	2.73
2.50E-02	5.89E-03	0.44	1.42E-04	-0.69	1.46E-03	0.40
1.25E-02	6.31E-03	-0.10	7.86E-05	0.86	1.57E-03	-0.10
6.25E-03	4.66E-03	0.44	3.28E-05	1.26	1.16E-03	0.44
3.13E-03	3.04E-03	0.62	1.22E-05	1.43	7.53E-04	0.62
1.56E-03	1.86E-03	0.71	4.20E-06	1.53	4.60E-04	0.71

case 4	**k**	**case 5**	**k**	**case 6**	**k**	**case 7**	**k**
1.04E-01	0.00	2.32E-01	0.00	1.47E-01	0.00	5.82E-02	0.00
2.57E-02	2.02	5.81E-02	2.00	3.60E-02	2.03	1.43E-02	2.02
3.88E-03	2.72	8.83E-03	2.72	5.43E-03	2.73	2.17E-03	2.72
2.91E-03	0.41	6.48E-03	0.45	4.06E-03	0.42	1.62E-03	0.42
3.14E-03	-0.11	6.96E-03	-0.10	4.35E-03	-0.10	1.74E-03	-0.10
2.32E-03	0.43	5.14E-03	0.44	3.21E-03	0.44	1.29E-03	0.44
1.51E-03	0.62	3.35E-03	0.62	2.09E-03	0.62	8.40E-04	0.62
9.26E-04	0.71	2.05E-03	0.71	1.28E-03	0.71	5.14E-04	0.71

Table A.2: The L^∞ errors for DDM1

ϵ	**case 1**	**k**	**case 2**	**k**	**case 3**	**k**
2.00E-01	3.42E-01	0.00	5.80E-02	0.00	4.44E-02	0.00
1.00E-01	1.70E-01	1.01	1.37E-02	2.09	2.28E-02	0.96
5.00E-02	8.45E-02	1.01	3.31E-03	2.04	1.16E-02	0.98
2.50E-02	4.17E-02	1.02	8.19E-04	2.02	5.84E-03	0.99
1.25E-02	2.07E-02	1.01	2.03E-04	2.01	2.93E-03	0.99
6.25E-03	1.03E-02	1.00	5.07E-05	2.00	1.47E-03	1.00
3.13E-03	5.16E-03	1.00	1.27E-05	2.00	7.35E-04	1.00
1.56E-03	2.58E-03	1.00	3.16E-06	2.00	3.68E-04	1.00

case 4	**k**	**case 5**	**k**	**case 6**	**k**	**case 7**	**k**
9.27E-02	0.00	3.74E-01	0.00	1.99E-01	0.00	5.26E-02	0.00
4.54E-02	1.03	1.79E-01	1.06	1.01E-01	0.97	2.60E-02	1.02
2.25E-02	1.02	8.77E-02	1.03	5.12E-02	0.99	1.29E-02	1.01
1.12E-02	1.00	4.30E-02	1.03	2.55E-02	1.01	6.44E-03	1.01
5.59E-03	1.00	2.13E-02	1.01	1.27E-02	1.00	3.21E-03	1.00
2.79E-03	1.00	1.06E-02	1.01	6.36E-03	1.00	1.60E-03	1.00
1.39E-03	1.00	5.29E-03	1.00	3.18E-03	1.00	8.02E-04	1.00
6.97E-04	1.00	2.64E-03	1.00	1.59E-03	1.00	4.01E-04	1.00

Table A.3: The L^2 errors for DDM2

ϵ	**case 1**	**k**	**case 2**	**k**	**case 3**	**k**
2.00E-01	1.65E-01	0.00	3.82E-02	0.00	3.53E-02	0.00
1.00E-01	7.95E-02	1.05	9.03E-03	2.08	1.81E-02	0.96
5.00E-02	3.88E-02	1.04	2.19E-03	2.04	9.11E-03	0.99
2.50E-02	1.91E-02	1.02	5.42E-04	2.02	4.61E-03	0.98
1.25E-02	9.51E-03	1.00	1.35E-04	2.01	2.33E-03	0.98
6.25E-03	4.82E-03	0.98	3.38E-05	2.00	1.19E-03	0.97
3.13E-03	2.40E-03	1.00	8.42E-06	2.00	5.93E-04	1.00
1.56E-03	1.20E-03	1.01	2.10E-06	2.00	2.96E-04	1.00

case 4	**k**	**case 5**	**k**	**case 6**	**k**	**case 7**	**k**
7.84E-02	0.00	1.94E-01	0.00	1.06E-01	0.00	4.34E-02	0.00
3.83E-02	1.03	9.08E-02	1.10	5.26E-02	1.01	2.13E-02	1.03
1.88E-02	1.03	4.36E-02	1.06	2.61E-02	1.01	1.05E-02	1.02
9.39E-03	1.00	2.13E-02	1.04	1.30E-02	1.01	5.22E-03	1.01
4.71E-03	0.99	1.06E-02	1.01	6.50E-03	1.00	2.62E-03	1.00
2.40E-03	0.97	5.34E-03	0.98	3.31E-03	0.98	1.33E-03	0.98
1.20E-03	1.00	2.66E-03	1.01	1.65E-03	1.00	6.64E-04	1.00
5.96E-04	1.01	1.32E-03	1.01	8.22E-04	1.01	3.31E-04	1.01

Table A.4: The L^∞ errors for DDM2

ϵ	**case 1**	**k**	**case 2**	**k**	**case 3**	**k**
2.00E-01	3.82E-02	0.00	1.37E-02	0.00	6.82E-03	0.00
1.00E-01	9.45E-02	-1.31	7.22E-03	0.92	1.44E-02	-1.08
5.00E-02	8.03E-02	0.24	3.12E-03	1.21	1.17E-02	0.30
2.50E-02	5.39E-02	0.58	1.19E-03	1.39	7.79E-03	0.59
1.25E-02	3.33E-02	0.69	4.18E-04	1.51	4.80E-03	0.70
6.25E-03	1.97E-02	0.76	1.40E-04	1.58	2.83E-03	0.76
3.13E-03	1.14E-02	0.79	4.49E-05	1.64	1.63E-03	0.80
1.56E-03	6.42E-03	0.82	1.43E-05	1.66	9.18E-04	0.83

case 4	**k**	**case 5**	**k**	**case 6**	**k**	**case 7**	**k**
1.10E-02	0.00	3.57E-02	0.00	2.61E-02	0.00	6.36E-03	0.00
2.59E-02	-1.23	9.39E-02	-1.39	6.02E-02	-1.21	1.50E-02	-1.23
2.16E-02	0.26	8.08E-02	0.22	5.02E-02	0.26	1.25E-02	0.26
1.46E-02	0.57	5.46E-02	0.56	3.35E-02	0.58	8.39E-03	0.57
9.01E-03	0.69	3.39E-02	0.69	2.06E-02	0.70	5.19E-03	0.69
5.34E-03	0.76	2.01E-02	0.75	1.22E-02	0.76	3.07E-03	0.76
3.07E-03	0.80	1.16E-02	0.79	7.02E-03	0.80	1.77E-03	0.80
1.74E-03	0.82	6.57E-03	0.82	3.96E-03	0.82	9.99E-04	0.82

Table A.5: The L^2 errors for DDM3

ϵ	**case 1**	**k**	**case 2**	**k**	**case 3**	**k**
2.00E-01	4.73E-02	0.00	9.52E-03	0.00	1.06E-02	0.00
1.00E-01	4.42E-02	0.10	4.92E-03	0.95	1.15E-02	-0.11
5.00E-02	3.66E-02	0.27	2.08E-03	1.24	9.17E-03	0.32
2.50E-02	2.44E-02	0.59	7.82E-04	1.41	6.08E-03	0.59
1.25E-02	1.50E-02	0.70	2.72E-04	1.52	3.73E-03	0.70
6.25E-03	8.84E-03	0.76	9.04E-05	1.59	2.20E-03	0.76
3.13E-03	5.09E-03	0.80	2.89E-05	1.64	1.26E-03	0.80
1.56E-03	2.87E-03	0.82	9.14E-06	1.66	7.12E-04	0.83

case 4	**k**	**case 5**	**k**	**case 6**	**k**	**case 7**	**k**
2.27E-02	0.00	5.44E-02	0.00	3.11E-02	0.00	1.26E-02	0.00
2.19E-02	0.06	4.75E-02	0.19	3.12E-02	-0.01	1.22E-02	0.04
1.80E-02	0.28	3.99E-02	0.25	2.54E-02	0.30	1.00E-02	0.28
1.21E-02	0.58	2.67E-02	0.58	1.68E-02	0.59	6.71E-03	0.58
7.45E-03	0.70	1.65E-02	0.70	1.03E-02	0.70	4.14E-03	0.70
4.40E-03	0.76	9.74E-03	0.76	6.09E-03	0.76	2.44E-03	0.76
2.53E-03	0.80	5.61E-03	0.79	3.50E-03	0.80	1.41E-03	0.80
1.43E-03	0.82	3.17E-03	0.82	1.98E-03	0.82	7.94E-04	0.82

Table A.6: The L^∞ errors for DDM3

Appendix B

Additional numerical results of mDDMs for 1D Poisson equations

We have tested the following three mDDMs using $h = \epsilon^{1.5}/4$:

mDDM1: $\nabla(\phi\nabla u) - \frac{1}{\epsilon^3}(1-\phi)(u - g - r\boldsymbol{n}\cdot\nabla u) = \phi f$,

mDDM2: $\phi\Delta u - \frac{1}{\epsilon^2}(1-\phi)(u - g - r\boldsymbol{n}\cdot\nabla u) = \phi f$,

mDDM3: $\nabla(\phi\nabla u) - \frac{1}{\epsilon^2}|\nabla\phi|(u - g - r\boldsymbol{n}\cdot\nabla u) = \phi f$,

on the seven cases given in Appendix A. The problem setup and the numerical discretization are analogous to those in Appendix A. In case 3-7, mDDM1-3 preform analogously as those in case 1. However in case 2, in which $A = 0$, we observe similar behaviour as those corresponding DDMs presented in Appendix A. Our analysis in Sec. 2.1.3.2 indicates $\bar{u}_1^{(1)}(0) \approx -A/2.92$ (Eq. (2.120)) and $\hat{u}_1^{(1)}(0) \approx Ae^{1/36}/2.92$ (Eq. (2.121)) for mDDM2, which both vanish when $A = 0$. Hence, mDDM2 can achieve 2nd order accuracy when $A = 0$. As for mDDM1 and mDDM3, the errors are again dominated by $\mathcal{O}(\epsilon^2(\ln(\epsilon))^2)$, whose coefficient is not affected by our modification in the next order matching when $A = 0$. In Fig. A.1(b),

we plot $D(\epsilon) = \lim_{z_2 \to -\infty}(u_\epsilon - u)/\epsilon^2$ versus $\ln(\epsilon)$ using the numerical solution of mDDM1 in case 2 and find that it is a quadratic function of $\ln(\epsilon)$.

ϵ	**case 1**	**k**	**case 2**	**k**	**case 3**	**k**
2.00E-01	4.88E-01	0.00	3.11E-02	0.00	7.00E-02	0.00
1.00E-01	1.50E-01	1.70	9.11E-03	1.77	2.19E-02	1.68
5.00E-02	4.46E-02	1.75	2.64E-03	1.79	6.57E-03	1.73
2.50E-02	1.26E-02	1.83	8.14E-04	1.70	1.87E-03	1.81
1.25E-02	3.34E-03	1.91	2.69E-04	1.60	5.05E-04	1.89
6.25E-03	8.61E-04	1.95	9.25E-05	1.54	1.33E-04	1.92

case 4	**k**	**case 5**	**k**	**case 6**	**k**	**case 7**	**k**
1.25E-01	0.00	4.81E-01	0.00	3.07E-01	0.00	7.37E-02	0.00
3.96E-02	1.66	1.49E-01	1.69	9.44E-02	1.70	2.31E-02	1.68
1.20E-02	1.73	4.45E-02	1.74	2.81E-02	1.75	6.94E-03	1.73
3.40E-03	1.82	1.25E-02	1.83	7.94E-03	1.82	1.97E-03	1.82
9.09E-04	1.90	3.31E-03	1.92	2.12E-03	1.90	5.25E-04	1.90
2.36E-04	1.95	8.44E-04	1.97	5.53E-04	1.94	1.36E-04	1.95

Table B.1: The L^2 errors for mDDM1

ϵ	**case 1**	**k**	**case 2**	**k**	**case 3**	**k**
2.00E-01	2.10E-01	0.00	2.06E-02	0.00	5.51E-02	0.00
1.00E-01	6.59E-02	1.67	5.93E-03	1.80	1.71E-02	1.69
5.00E-02	1.98E-02	1.74	1.70E-03	1.80	5.12E-03	1.74
2.50E-02	5.58E-03	1.83	5.22E-04	1.70	1.45E-03	1.82
1.25E-02	1.55E-03	1.85	1.72E-04	1.60	3.92E-04	1.89
6.25E-03	4.91E-04	1.65	5.91E-05	1.54	1.22E-04	1.68

case 4	**k**	**case 5**	**k**	**case 6**	**k**	**case 7**	**k**
1.05E-01	0.00	2.26E-01	0.00	1.49E-01	0.00	5.85E-02	0.00
3.29E-02	1.67	7.11E-02	1.67	4.64E-02	1.68	1.83E-02	1.67
9.90E-03	1.73	2.14E-02	1.73	1.39E-02	1.74	5.51E-03	1.73
2.81E-03	1.82	6.01E-03	1.83	3.94E-03	1.82	1.56E-03	1.82
7.71E-04	1.86	1.70E-03	1.82	1.07E-03	1.88	4.28E-04	1.87
2.45E-04	1.65	5.42E-04	1.65	3.39E-04	1.66	1.36E-04	1.65

Table B.2: The L^∞ errors for mDDM1

ϵ	**case 1**	**k**	**case 2**	**k**	**case 3**	**k**
2.00E-01	2.85E-01	0.00	3.73E-02	0.00	3.75E-02	0.00
1.00E-01	1.41E-01	1.01	8.77E-03	2.09	1.92E-02	0.97
5.00E-02	6.98E-02	1.01	2.13E-03	2.04	9.70E-03	0.98
2.50E-02	3.46E-02	1.01	5.24E-04	2.02	4.88E-03	0.99
1.25E-02	1.73E-02	1.00	1.30E-04	2.01	2.45E-03	1.00
6.25E-03	8.62E-03	1.00	3.23E-05	2.01	1.23E-03	1.00

case 4	**k**	**case 5**	**k**	**case 6**	**k**	**case 7**	**k**
7.65E-02	0.00	3.07E-01	0.00	1.68E-01	0.00	4.36E-02	0.00
3.77E-02	1.02	1.48E-01	1.05	8.48E-02	0.98	2.16E-02	1.01
1.87E-02	1.01	7.23E-02	1.03	4.25E-02	1.00	1.08E-02	1.01
9.33E-03	1.00	3.57E-02	1.02	2.12E-02	1.00	5.37E-03	1.00
4.66E-03	1.00	1.77E-02	1.01	1.06E-02	1.00	2.68E-03	1.00
2.33E-03	1.00	8.84E-03	1.00	5.31E-03	1.00	1.34E-03	1.00

Table B.3: The L^2 errors for mDDM2

ϵ	**case 1**	**k**	**case 2**	**k**	**case 3**	**k**
2.00E-01	1.33E-01	0.00	2.50E-02	0.00	2.96E-02	0.00
1.00E-01	6.48E-02	1.04	5.86E-03	2.09	1.52E-02	0.96
5.00E-02	3.19E-02	1.02	1.42E-03	2.05	7.67E-03	0.98
2.50E-02	1.59E-02	1.01	3.52E-04	2.01	3.88E-03	0.98
1.25E-02	7.93E-03	1.00	8.73E-05	2.01	1.95E-03	1.00
6.25E-03	3.96E-03	1.00	2.18E-05	2.00	9.77E-04	1.00

case 4	**k**	**case 5**	**k**	**case 6**	**k**	**case 7**	**k**
6.43E-02	0.00	1.55E-01	0.00	8.67E-02	0.00	3.56E-02	0.00
3.17E-02	1.02	7.35E-02	1.07	4.34E-02	1.00	1.76E-02	1.02
1.57E-02	1.01	3.57E-02	1.04	2.16E-02	1.00	8.73E-03	1.01
7.89E-03	1.00	1.77E-02	1.02	1.09E-02	1.00	4.38E-03	1.00
3.94E-03	1.00	8.78E-03	1.01	5.43E-03	1.00	2.19E-03	1.00
1.97E-03	1.00	4.39E-03	1.00	2.72E-03	1.00	1.09E-03	1.00

Table B.4: The L^∞ errors for mDDM2

ϵ	**case 1**	**k**	**case 2**	**k**	**case 3**	**k**
2.00E-01	1.55E-01	0.00	3.89E-02	0.00	2.80E-02	0.00
1.00E-01	3.77E-02	2.04	1.38E-02	1.50	7.15E-03	1.97
5.00E-02	8.54E-03	2.14	4.87E-03	1.50	1.80E-03	1.99
2.50E-02	1.89E-03	2.17	1.72E-03	1.50	4.71E-04	1.94
1.25E-02	4.16E-04	2.19	5.88E-04	1.55	1.27E-04	1.89
6.25E-03	8.74E-05	2.25	1.94E-04	1.60	3.46E-05	1.88

case 4	**k**	**case 5**	**k**	**case 6**	**k**	**case 7**	**k**
4.42E-02	0.00	1.44E-01	0.00	1.07E-01	0.00	2.57E-02	0.00
1.08E-02	2.03	3.31E-02	2.12	2.69E-02	1.99	6.31E-03	2.02
2.51E-03	2.10	6.78E-03	2.29	6.50E-03	2.05	1.48E-03	2.09
5.86E-04	2.10	1.25E-03	2.44	1.59E-03	2.03	3.48E-04	2.09
1.38E-04	2.09	1.91E-04	2.71	4.01E-04	1.99	8.28E-05	2.07
3.20E-05	2.11	1.39E-05	3.78	1.01E-04	1.98	1.96E-05	2.08

Table B.5: The L^2 errors for mDDM3

ϵ	**case 1**	**k**	**case 2**	**k**	**case 3**	**k**
2.00E-01	8.23E-02	0.00	2.58E-02	0.00	2.18E-02	0.00
1.00E-01	2.23E-02	1.88	8.98E-03	1.52	5.82E-03	1.91
5.00E-02	5.96E-03	1.91	3.14E-03	1.51	1.56E-03	1.90
2.50E-02	2.03E-03	1.55	1.10E-03	1.51	5.17E-04	1.59
1.25E-02	6.15E-04	1.72	3.76E-04	1.55	1.56E-04	1.73
6.25E-03	2.29E-04	1.42	1.24E-04	1.60	5.73E-05	1.44

case 4	**k**	**case 5**	**k**	**case 6**	**k**	**case 7**	**k**
4.10E-02	0.00	8.94E-02	0.00	5.78E-02	0.00	2.29E-02	0.00
1.12E-02	1.88	2.40E-02	1.89	1.58E-02	1.88	6.22E-03	1.88
2.99E-03	1.90	6.39E-03	1.91	4.22E-03	1.90	1.67E-03	1.90
1.02E-03	1.56	2.21E-03	1.53	1.41E-03	1.58	5.64E-04	1.56
3.07E-04	1.72	6.72E-04	1.72	4.27E-04	1.73	1.71E-04	1.72
1.14E-04	1.43	2.52E-04	1.41	1.58E-04	1.43	6.35E-05	1.43

Table B.6: The L^∞ errors for mDDM3

Appendix C

Validation of the asymptotic analysis

Here we present validations of our asymptotic analysis using the numerical results for the seven cases in Appendix A. In Tab. C.1, we present $\bar{u}_1^{(1)}$s in DDM2 obtained from both our asymptotic analysis theory (Eq. (2.42)) and the numerical results. In Tab. C.2, we compare the slope $C(\epsilon)$ computed numerically (through an analogous linear fit as in Sec. 2.1.2.2) with the one derived from our asymptotic analysis theory ($-A/6$) for DDM1 and DDM3. In Tab. C.3, we show $\hat{u}_3^{(1.5)}(0)$s from our asymptotic theory ($-A/\sqrt{2\pi}$ for mDDM1 and $-A/\sqrt{6\pi}$ for mDDM3) together with the ones calculated from the numerical results for mDDM1 and mDDM3. $\bar{u}_1^{(1)}$ and $\hat{u}^{(1)}(0)$ in mDDM2 obtained from both our asymptotic analysis theory (Eqs. (2.120) and (2.121)) and the numerical results are presented in Tab. C.4. Clearly our theory is consistent with the numerical results.

case	**Theory**	**Numeric**
case 1	-0.450	-0.450
case 2	0.000	0.000
case 3	0.180	0.183
case 4	0.363	0.368
case 5	-4.020	-4.072
case 6	-0.403	-0.408
case 7	-0.301	-0.305

Table C.1: Comparisons between $\bar{u}_1^{(1)}$ from theory and the one from numerical results.

case	**Theory**	**Numeric (DDM1)**	**Numeric (DDM3)**
case 1	-0.185	-0.186	-0.188
case 2	0.000	0.000	0.000
case 3	0.074	0.075	0.075
case 4	0.149	0.150	0.152
case 5	-1.655	-1.667	-1.686
case 6	-0.166	-0.167	-0.168
case 7	-0.124	-0.125	-0.126

Table C.2: Comparisons between the slope of $C(\epsilon)$ from theory and the one from numerical results.

	mDDM1		mDDM3	
case	Theory	Numeric	Theory	Numeric
case 1	-0.443	-0.442	-0.256	-0.257
case 2	0.000	0.001	0.000	-0.001
case 3	0.178	0.177	0.103	0.103
case 4	0.356	0.357	0.206	0.207
case 5	-3.961	-3.952	-2.287	-2.299
case 6	-0.397	-0.396	-0.229	-0.230
case 7	-0.297	-0.296	-0.171	-0.172

Table C.3: Comparisons between $\hat{u}_3^{(1.5)}(0)$ from asymptotic theory and from numerical results of mDDM1 and mDDM3.

	$\bar{u}^{(1)}(0)$		$\hat{u}^{(1)}(0)$	
case	Predictions	Numerics	Predictions	Numerics
case 1	-0.381	-0.380	-0.391	-0.391
case 2	0.000	0.000	0.000	0.000
case 3	0.152	0.152	0.157	0.157
case 4	0.307	0.307	0.316	0.315
case 5	-3.401	-3.399	-3.496	-3.495
case 6	-0.341	-0.340	-0.350	-0.350
case 7	-0.255	-0.254	-0.262	-0.262

Table C.4: Comparisons between the asymptotic theory and the numerical results for $\bar{u}^{(1)}(0)$ and $\hat{u}^{(1)}(0)$ of mDDM2.

Appendix D

Derivation of solution to Eq. (2.109)

Recall the homogeneous ordinary differential equation (Eq. (2.109)),

$$y'' - e^{6x}(y - xy') = 0.$$

Clearly, $y_1 = x$ is one of the linearly independent solution to Eq. (2.109). We derive the other solution through reduction of order. We assume $y_2(x) = v(x)y_1(x) = xv(x)$ and plug into Eq. (2.109). Thus,

$$xv'' + 2v' + x^2 e^{6x} v' = 0, \tag{D.1}$$

which gives $v(x) = \int \frac{e^{e^{6x}(1-6x)/36}}{x^2} dx$ for $x \neq 0$. Hence,

$$y_2 = x \int \frac{e^{e^{6x}(1-6x)/36}}{x^2} dx = -e^{e^{6x}(1-6x)/36} - x \int h(x)dx \text{ for } x \neq 0, \tag{D.2}$$

where $h(x) = e^{e^{6x}(1-6x)/36+6x}$. It is not hard to verify that y_2 is a solution to Eq. (2.109) for all x including 0. Although the anti-derivative of $h(x)$ is not an elementary function, $h(x) \in L^1(-\infty, +\infty)$ and Matlab computes $\int_{-\infty}^{+\infty} h(x)dx \approx 2.92$. Let $H'(x) = h(x)$ and y_2

can be written as

$$y_2 = -e^{e^{6x}(1-6x)/36} - x\int_0^x h(t)dt - H(0)x. \tag{D.3}$$

Note that $H(0)x$ is linearly dependent with respect to y_1, thus y_2 can be simplified as

$$y_2 = -e^{e^{6x}(1-6x)/36} - x\int_0^x h(t)dt. \tag{D.4}$$

Hence, the general solution to Eq. (2.109) is

$$y = C_1 x + C_2(-e^{e^{6x}(1-6x)/36} - x\int_0^x h(t)dt). \tag{D.5}$$